Chemical Science

ROYAL SOCIETY OF CHEMISTRY

EDGE ARTICLE

View Article Online
View Journal | View Issue

Cite this: *Chem. Sci.*, 2022, **13**, 13426

All publication charges for this article have been paid for by the Royal Society of Chemistry

A long-lived charge-separated state of spiro compact electron donor–acceptor dyads based on rhodamine and naphthalenediimide chromophores†

Xiao Xiao, ‡[a] Ivan Kurganskii,‡[b] Partha Maity, ‡[c] Jianzhang Zhao, *[ad] Xiao Jiang,*[e] Omar F. Mohammed*[c] and Matvey Fedin *[b]

Spiro rhodamine (Rho)-naphthalenediimide (**NDI**) electron donor–acceptor orthogonal dyads were prepared to generate a long-lived charge separation (CS) state based on the electron spin control approach, *i.e.* to form the ^{3}CS state, not the ^{1}CS state, to prolong the CS state lifetime by the electron spin forbidden feature of the charge recombination process of ^{3}CS → S_0. The electron donor Rho (lactam form) is attached *via* three σ bonds, including two C–C and one N–N bonds (**Rho-NDI**), or an intervening phenylene, to the electron acceptor **NDI** (**Rho-Ph-NDI** and **Rho-PhMe-NDI**). Transient absorption (TA) spectra show that fast intersystem crossing (ISC) (<120 fs) occurred to generate an upper triplet state localized on the **NDI** moiety (^{3}NDI*), and then to form the CS state. For **Rho-NDI** in both non-polar and polar solvents, a long-lived ^{3}CS state (lifetime $\tau = 0.13$ μs) and charge separation quantum yield (Φ_{CS}) up to 25% were observed, whereas for **Rho-Ph-NDI** ($\tau_T = 1.1$ μs) and **Rho-PhMe-NDI** ($\tau_T = 2.0$ μs), a low-lying ^{3}NDI* state was formed by charge recombination (CR) in *n*-hexane (HEX). In toluene (TOL), however, CS states were observed for **Rho-Ph-NDI** (0.37 μs) and **Rho-PhMe-NDI** (0.63 μs). With electron paramagnetic resonance (EPR) spectra, weak electronic coupling between the Rho and **NDI** moieties for **Rho-NDI** was proved. Time-resolved EPR (TREPR) spectra detected two transient species including **NDI**-localized triplets (formed *via* SOC-ISC) and a ^{3}CS state. The CS state of **Rho-NDI** features the largest dipolar interaction ($|D| = 184$ MHz) compared to **Rho-Ph-NDI** ($|D| = 39$ MHz) and **Rho-PhMe-NDI** ($|D| = 41$ MHz) due to the smallest distance between Rho and **NDI** moieties. For **Rho-NDI**, the time-dependent *e,a* → *a,e* phase change of the CS state TREPR spectrum indicates that the long-lived CS state is based on the electron spin control effect.

Received 30th July 2022
Accepted 25th October 2022

DOI: 10.1039/d2sc04258d

rsc.li/chemical-science

Introduction

Charge separation (CS) is important in the study of fundamental photochemistry,[1–10] and in the areas of artificial photosynthesis,[11] photocatalysis and organic photovoltaics (OPVs),[12–15] *etc.* The interaction between the locally excited (LE) and CS states in electron donor–acceptor systems plays an important role in OPVs and organic light-emitting diodes (OLEDs).[16] Concerning CS, a few key factors are the CS quantum yields (Φ_{CS}), the CS state energy and the lifetimes.[17–19] The intermolecular electron transfer initiated by the photo-generated CS state can be enhanced by higher CS state energy and longer CS state lifetime. The electron transfer rate constant, especially in weakly coupled systems, is described by eqn (1), based on Marcus theory for electron transfer:

$$k_{ET} = \left(\frac{4\pi^3}{h^2 \lambda k_B T}\right)^{1/2} V^2 \exp\left[-\frac{\left(\Delta G^0_{ET} + \lambda\right)^2}{4\lambda k_B T}\right] \quad (1)$$

where h and k_B represent the Planck and Boltzmann constants, respectively. ΔG^0_{ET} is the Gibbs free energy change of the

[a]*State Key Laboratory of Fine Chemicals, Frontiers Science Center for Smart Materials, School of Chemical Engineering, Dalian University of Technology, Dalian 116024, P. R. China. E-mail: zhaojzh@dlut.edu.cn*

[b]*International Tomography Center, SB RAS Institutskaya Str., 3A, and Novosibirsk State University, Pirogova str. 2, Novosibirsk 630090, Russia. E-mail: mfedin@tomo.nsc.ru*

[c]*Division of Physical Sciences and Engineering, King Abdullah University of Science and Technology (KAUST), Thuwal 23955-6900, Kingdom of Saudi Arabia. E-mail: omar.abdelsaboor@kaust.edu.sa*

[d]*State Key Laboratory of Chemistry and Utilization of Carbon Based Energy Resources, College of Chemistry, Xinjiang University, Urumqi 830017, P. R. China*

[e]*Key Laboratory of Industrial Ecology and Environmental Engineering (Ministry of Education), School of Environmental Science and Technology, Dalian University of Technology, Dalian 116024, P. R. China. E-mail: xjiang@dlut.edu.cn*

† Electronic supplementary information (ESI) available: General experimental methods, synthesis of compounds, molecular structure characterization, X-ray crystallographic data, computational details and additional spectra. CCDC 2190442. For ESI and crystallographic data in CIF or other electronic format see https://doi.org/10.1039/d2sc04258d

‡ These authors contributed equally to this work.

electron transfer, λ is the total reorganization energy, and V is the electronic matrix element.

Based on the equation, a few methods have been studied to prolong the CS state lifetimes. In conventional electron donor–acceptor dyads containing a long linker and multiple donors (or acceptors), the electronic coupling is weak, and thus the CS state lifetime can be prolonged.[4,20,21] The systems with this strategy also show high Φ_{CS}.[22,23] Another method to prolong the CS state lifetime is to exploit the so-called Marcus inverted region effect, *i.e.* to attain a CS state with high energy so that the Gibbs free energy change (ΔG^0_{CR}) of the charge recombination (CR) process is larger than the reorganization energy (λ) ($-\Delta G^0_{CR} > \lambda$). However, these conventional methods suffer from drawbacks. For instance, the large separation of the donor and the acceptor, or the use of multiple donors (or acceptors), makes the synthesis challenging, and the CS state may have a low energy. For the exploitation of the Marcus inverted region effect, a donor or acceptor with small λ is required, but the availability of such a donor or acceptor is limited (C_{60} is one example).[4] On the other hand, the high CS state energy pushes the absorption wavelength to the blue or UV spectral range, and clearly these are disadvantages for the application of electron donor–acceptor dyads in photocatalysis and OPVs.[1,24]

Another less investigated method to prolong the CS state lifetimes is electron spin control in CS and CR processes.[1,25–29] As other photophysical processes, the CS and CR processes are also electron spin selective, *i.e.* the electron spin is conserved in these processes. That is, the formation of the ^{1}CS state with a localized singlet excited state (*i.e.* ^{1}LE state) as the precursor is bound to prevail compared to the formation of the ^{3}CS state.[1,25–30] On the other hand, the CR of $^1\text{CS} \rightarrow S_0$ is electron spin allowed, whereas the CR of $^3\text{CS} \rightarrow S_0$ is electron spin forbidden, and thus the ^{3}CS state should be inherently longer lived than the ^{1}CS state. Therefore, it is desired to attain the ^{3}CS state, in order to prolong the CS state lifetime.[1] However, the conventional electron donor–acceptor dyads have a large separation distance between the donor and acceptor, and thus the electron exchange integral (J) of the electrons in the frontier molecular orbitals of the CS state is extremely small (<0.01 cm^{-1}), and as a result, no stable ^{1}CS or ^{3}CS states can be formed, and very often it is a spin-correlated radical pair (SCRP).[1,25,31,32] Since a fraction of the population of SCRP is in the singlet state, the CR channel will shorten the lifetime of the CS state. The potential of the electron spin control method to prolong the CS state lifetime is not maximized under these circumstances. Moreover, it is critical to firstly produce the ^{3}LE state precursor for the subsequent formation of the ^{3}CS state.[1] Thus, transition metal coordination frameworks (known for their ultrafast, efficient ISC)[5,26,27,30,33] or organic chromophores with inherent ISC are required.[19,28,34–38] However, these approaches suffer from high synthesis cost and limited availability of appropriate chromophores.

One method to tackle the above challenge is to prepare a compact electron donor–acceptor dyad, *i.e.* using a short linker between the donor and acceptor.[1,39] Thus, the J value is larger compared with that of the dyads with a long distance between the donor and acceptor, and the formation of ^{1}CS and ^{3}CS states becomes possible. Only in this case the potential of the electron spin control for the prolongation of the CS state lifetime can be exploited.[29] Concerning this circumstance, one critical issue is the production of the ^{3}LE state firstly in these heavy atom-free compounds.[3,24,40] Recently we used the electron spin control strategy in a compact rhodamine (Rho)-naphthalimide (NI) dyad to attain a long-lived ^{3}CS state, with femtosecond, subnanosecond and nanosecond transient absorption spectroscopic methods, and we unravelled the photophysical processes as $S_0 \rightarrow {}^1\text{LE} \rightarrow {}^1\text{CS} \rightarrow {}^3\text{NI} \rightarrow {}^3\text{CS} \rightarrow S_0$, and the CS state lifetime was determined to be 0.94 μs in fluid solution at room temperature.[39] Recently we used pyromellitimide to prepare rhodamine derivatives, and a CS state lifetime of 2.6 μs was observed.[41] It should be pointed out that the closed form of the Rho unit was rarely used as an electron donor for the preparation of compact electron donor–acceptor dyads. The advantage of this novel electron donor ($E_{OX} = +0.52$ V, *vs.* Fc/Fc$^+$) is the sterically congested microenvironment created by it,[42] which is helpful for the donor and acceptor to adopt a rigid orthogonal geometry, beneficial for spin–orbit charge transfer intersystem crossing (SOCT-ISC), a novel method to generate the ^{3}LE state as the precursor of CS, so that the ^{3}CS state can be formed, and the electron spin control method can be implemented.[24,39]

In order to fully exploit this strategy, herein we prepared a series of Rho-naphthalenediimide (**NDI**) dyads (Scheme 1), to study the CS and CR processes, especially the effect of the molecular structure and geometry on the CS state lifetimes. In the three target dyads we prepared, the distance between the donor and acceptor is varied, by a direct connection of the donor and acceptor (**Rho-NDI**) or using an intervening phenyl link between the two units (**Rho-Ph-NDI**). Furthermore, the electronic coupling between the donor and acceptor is also varied *via* conformation restriction by the methyl groups on the intervening phenyl unit between the donor and acceptor (**Rho-PhMe-NDI**). Steady state and time-resolved transient optical and magnetic spectroscopic methods were used for the study of the photophysical properties of the dyads.

Results and discussion

Molecular structure design and synthesis

The closed form of Rho is an electron donor ($E_{OX} = +0.52$ V, *vs.* Fc/Fc$^+$). The unique feature is the spiro structure and the steric hindered microenvironment when an electron acceptor attached.[39,42,43] **NDI** was used as the electron acceptor ($E_{RED} = -1.02$ V, *vs.* Fc/Fc$^+$).[44–46] The compact structure of **Rho-NDI** is beneficial for increasing the J magnitude, and to reduce the λ values.[47] We also prepared two analogues with an intervening phenyl linker inserted between the donor and acceptor (**Rho-Ph-NDI** and **Rho-PhMe-NDI**). The larger distance between the donor and acceptor in these two dyads may increase the CS state energy.[31] Moreover, the conformation restriction is also varied by the methyl groups attached on the intervening phenyl linker. This character may also have an effect on the CS, CR and the CS state lifetimes.

The synthesis of the compounds is based on the routine derivatization chemistry of Rho and **NDI** chromophores.[39,42] The yields are generally satisfactory. The molecular structures are verified by ^{1}H NMR, ^{13}C NMR, HR MS and Fourier transform infrared (FT-IR) spectral methods.

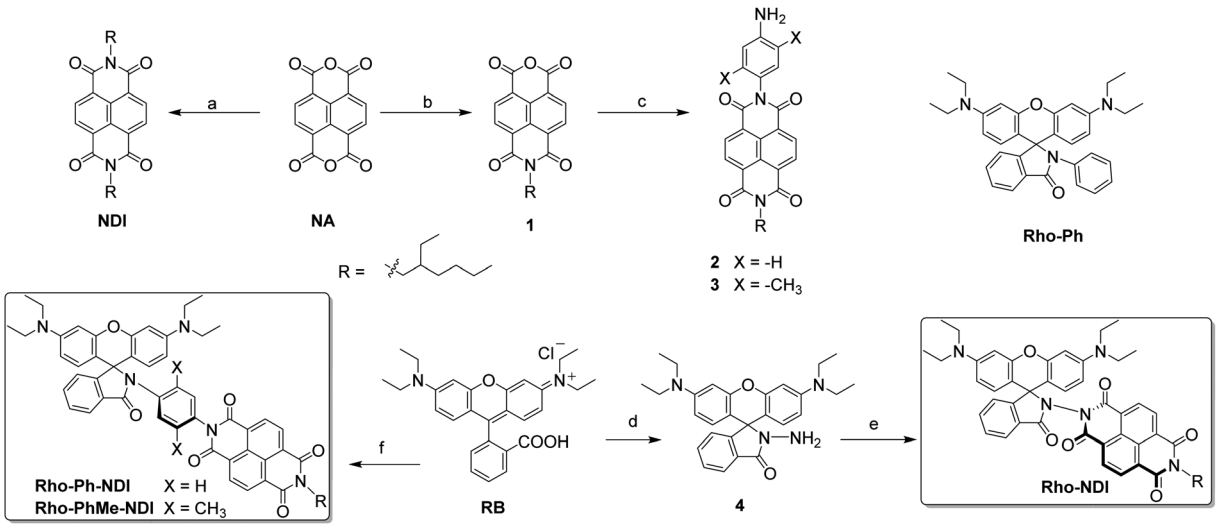

Scheme 1 Molecular structures of the dyads **Rho-NDI**, **Rho-Ph-NDI**, and **Rho-PhMe-NDI** and reference compounds. (a) 2-Ethylhexylamine, DMF, N_2, 150 °C, 12 h, and yield: 44%; (b) 2-ethylhexylamine, KOH, H_3PO_4, H_2O, N_2, 110 °C, 16 h, and yield: 40%; (c) 1,4-phenylenediamine or 2,5-dimethyl-1,4-phenylenediamine, DMF, N_2, 160 °C, 7 h, and yield: 21% or 60%; (d) $NH_2NH_2{\cdot}H_2O$, EtOH, N_2, reflux, 4.5 h, and yield: 86%; (e) **1**, AcOH, N_2, reflux, 24 h, and yield: 31%; (f) firstly, $POCl_3$, dry dichloromethane (DCM), N_2, reflux, and 5 h; then **2** or **3**, ACN, Et_3N, N_2, reflux, 21 h, and yield: 54% or 51%.

Single crystals of **Rho-NDI** were obtained by slow diffusion of *n*-hexane (HEX) into a tetrahydrofuran (THF) solution of the compound. X-ray diffraction shows that the centroid-to-centroid distance between xanthene and **NDI** units is 5.8 Å and the dihedral angle between the xanthene and **NDI** units is 52.9° (Fig. 1).

UV-visible absorption and luminescence emission studies

The UV-vis absorption spectra of the compounds were studied (Fig. 2a). **NDI** gives the featured absorption band in the range of 300–400 nm, which shows significant vibration progression. **Rho-Ph** shows absorption at 308 nm. All the dyads show UV-vis absorption spectra, which are identical to the sum of the absorption spectra of the **NDI** and the **Rho-Ph** units, and thus the electronic coupling between the donor and acceptor is negligible at the ground state,[18,48–50] because the *p*-xylene linker is known to be able to electronically isolate the donor and acceptor.[18] Given that the electronic coupling between the donor and acceptor was strong, a charge transfer (CT) absorption band ($S_0 \rightarrow {}^1$CT transition) should be observed.[50–52] It is interesting that even for **Rho-NDI**, in which the donor and acceptor are separated by three σ bonds, and the electronic coupling at the ground state is weak.

The Rho moiety is well known for the reversible spirolactam ↔ amide transformation in the presence of an acid or base.[53–55]

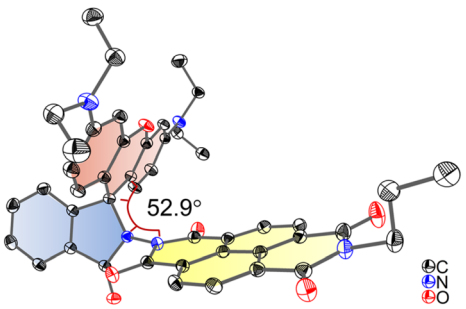

Fig. 1 ORTEP view of the molecular structure of **Rho-NDI** determined by single-crystal X-ray diffraction. Hydrogen atoms are omitted for clarity. Thermal ellipsoids are set at 50% probability. Deposition number 2190442 contains the supplementary crystallographic data for this paper. Note that to grow a single crystal, we prepared the analogue of **Rho-NDI** with *n*-propylamine, instead of 2-ethylhexylamine, for better crystallizability.

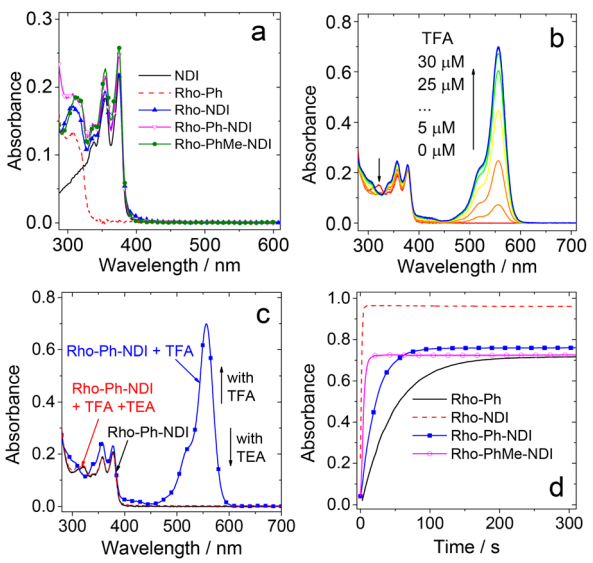

Fig. 2 (a) UV-vis absorption spectra of the compounds in *n*-hexane (HEX). UV-vis absorption spectra of **Rho-Ph-NDI** (b) with increasing amount of trifluoroacetic acid (TFA) added and (c) with the addition of TFA (c = 50 μM) or trimethylamine (TEA. neat, 10 μL) in MeOH. (d) Kinetics of the lactam → opened amide transformation of the Rho moiety for these compounds, monitored at 557 nm upon addition of TFA (c = 50 μM) in MeOH. $c = 1.0 \times 10^{-5}$ M. 25 °C.

For **Rho-Ph** and the dyads, upon addition of trifluoroacetic acid (TFA), an absorption band at 557 nm appeared, which is attributed to the opened amide form of Rho derivatives (Fig. 2b). The absorption band of the open form of Rho decreased with the addition of a base such as triethylamine (TEA) (Fig. 2c), indicating that the opening-closure reaction in the presence of an acid or base is reversible. The reaction kinetics (*i.e.* the absorption variation of **Rho-Ph** and the dyads at 557 nm) with the addition of TFA were also studied (Fig. 2d). **Rho-Ph** shows the slowest kinetics of lactam → open form transformation, for which the apparent transformation rate constant is $k = 2.2 \times 10^{-2}$ s^{-1}, followed by **Rho-Ph-NDI** ($k = 4.6 \times 10^{-2}$ s^{-1}). **Rho-NDI** ($k = 0.77$ s^{-1}) and **Rho-PhMe-NDI** ($k = 0.22$ s^{-1}) which show relatively faster kinetics (these values may be dependent on the acid concentration).

The photoluminescence of the compounds was studied (Fig. 3). In HEX, all the compounds show LE fluorescence emission bands in the range of 350–550 nm (Fig. 3a). The dyads give a broad and weak fluorescence emission band in the range of 650–850 nm. Neither the Rho nor the **NDI** unit gives a fluorescence emission band in this region, and thus it is attributed to a CS fluorescence emission band (^{1}CS → S$_0$), indicating the non-negligible electronic interaction of the radical anion and cation at the CS state. For **Rho-NDI**, the CS state decays with a biexponential feature, and the lifetime is 0.09 ns (91.2%)/2.91 ns (8.8%) in HEX (Fig. S20†). The biexponential decay of the CS state can be tentatively attributed to the existence of a dark ^{3}CS state and the equilibrium between ^{1}CS and ^{3}CS states. The similar energy of ^{1}CS and ^{3}CS states can be verified by the small $|J|$ value obtained by fitting TREPR spectra (see the later section). The species with a shorter lifetime is assigned to the prompt ^{1}CS state. The minor species with a longer lifetime is tentatively assigned to the ^{1}CS state originating from the dark ^{3}CS state. Similar results were observed for the decay of the CS states of **Rho-Ph-NDI** and **Rho-PhMe-NDI**, and the lifetimes were determined to be 0.32 ns (60.3%)/3.13 ns (39.7%) and 0.40 ns (76.3%)/3.90 ns (23.7%), respectively. In acetonitrile (ACN), only the LE fluorescence band was observed (Fig. 3b). In toluene (TOL), much stronger fluorescence for **NDI** was observed. One possible reason is the formation of exciplexes of **NDI** with TOL (Fig. S19†).[56] For the dyads, the fluorescence is very weak and no CS state fluorescence band was observed in TOL (Fig. S19†).

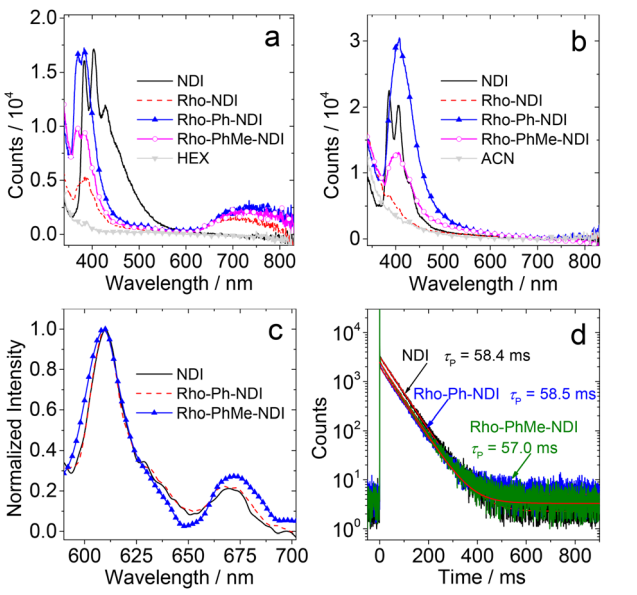

Fig. 3 Fluorescence emission spectra of the compounds in (a) HEX and (b) ACN. Optically matched solutions were used (all the solutions show the same absorbance at the excitation wavelength, λ_{ex} = 300 nm, and $A_{300\ nm} = 0.1$) and 25 °C. Emission bands below 350 nm in (a) and (b) are due to the Raman scattering of the solvent. (c) Normalized phosphorescence spectra of the compounds **NDI**, **Rho-Ph-NDI** and **Rho-PhMe-NDI** and (d) the corresponding phosphorescence decay traces of the compounds at 610 nm at 77 K in MeTHF. λ_{ex} = 370 nm. $c = 1.0 \times 10^{-4}$ M.

In order to determine the ^{3}NDI* energy of the compounds, the phosphorescence emission spectra in frozen solution at 77 K were studied (Fig. 3c). Phosphorescence emission bands in the range of 600–700 nm were observed under these conditions. Based on the identical results observed for **NDI** and the dyads, the phosphorescence bands are assigned to the ^{3}NDI* moiety. From the on-set of the phosphorescence band on the high energy side (can be approximated as the vibrational 00 transition of T$_1$ → S$_0$ radiative relaxation), the ^{3}NDI* state energy is approximated to be 2.04 eV, which is consistent with the previously reported phosphorescence spectrum for **NDI** (substituted with *n*-hexyl at the *N* position) in 2-methyltetrahydrofuran (MeTHF) at 77 K (2.04 eV).[57] The phosphorescence lifetimes were determined to be *ca.* 58 ms (Fig. 3d). However, no phosphorescence was observed for **Rho-NDI** at 77 K, even in the presence of ethyl iodide (in TOL/MeTHF/ethyl iodide, 3 : 1 : 2, v/v), and the possible reason is that the ^{3}CS state is the lowest-lying state rather than the ^{3}NDI* state. This postulate is supported by the calculated CS state energy with the Rehm–Weller equation (see the later section). Note that the ^{3}CS state should be weakly emissive, even at cryogenic temperature, due to the poor orbital overlap of the ^{3}CS → S$_0$ transition and the inhibited vibronic coupling. The photophysical parameters of the compounds are summarized in Table 1.

Electrochemical studies

The redox potentials of the compounds were studied by using cyclic voltammograms (Fig. 4a). **NDI** shows two reversible reduction waves at −1.02 V and −1.46 V (*vs.* Fc/Fc$^+$), respectively. No oxidation waves were observed in the redox potential window applied. These results are similar to previous reports on **NDI**.[56] For Rho-Ph, two pseudo-reversible oxidation waves at +0.52 V and +0.66 V were observed (*vs.* Fc/Fc$^+$), which is similar to a previously reported Rho-NI dyad.[39] These results indicate that the Rho unit acts as an electron donor and the **NDI** moiety acts as an electron acceptor in the dyads upon photoexcitation. For the dyads, the reduction potential is similar to that of **NDI**, whereas the oxidation potential is similar to that of Rho, indicating that the electronic interaction between the two units at the ground state is weak. The redox potentials are summarized in Table 2.

Based on the electrochemical data, the spectral data and the theoretical computation results (see the later section), the driving force of the possible photo-induced CS, *i.e.* the Gibbs free energy changes of the CS (ΔG^0_{CS}), was calculated with the Rehm–Weller equation (for details, please refer to the ESI†):[58]

Table 1 The photophysical properties of the compounds[a]

Compounds	λ_{abs}[b] (ε[c]) Lactam form	Open form[d]	λ_F[e]	Φ_F[f]	τ_F[g]	k_r[h]	k_{nr}[i]	λ_P[j]	τ_P[k]	Φ_{CS}[l]
NDI	375 (2.19)[m]	—[m]	403	0.5	0.29 (93.5%)/3.22 (6.5%)	1.04	2.07	609	58.4	—[m]
Rho-Ph	308 (1.35)	556 (7.16)	410[n]	1.2[n]	4.7[n]	0.26	0.21	—[o]	—[o]	—[m]
Rho-NDI	374 (2.20)	557 (9.61)	388/730	0.2	0.09 (91.2%)/2.91 (8.8%)	0.59	2.94	—[o]	—[o]	25
Rho-Ph-NDI	375 (2.48)	557 (7.59)	383/745	0.5	0.32 (60.3%)/3.13 (39.7%)	0.51	1.01	609	58.5	19[p]
Rho-PhMe-NDI	374 (2.59)	557 (7.24)	385/728	0.3	0.40 (76.3%)/3.90 (23.7%)	0.24	0.81	610	57.0	17[p]

[a] In HEX. [b] Maximal UV-vis absorption wavelength. $c = 1.0 \times 10^{-5}$ M, in nm. [c] Molar absorption coefficient, in 10^4 M^{-1} cm^{-1}. [d] In MeOH. [e] Maximal fluorescence emission wavelength, in nm. [f] Fluorescence quantum yields, in %. [g] Fluorescence lifetimes ($\lambda_{ex} = 340$ nm) of **NDI** at 420 nm, **Rho-NDI** at 710 nm, **Rho-Ph-NDI** and **Rho-PhMe-NDI** at 750 nm. $c = 1.0 \times 10^{-5}$ M, in ns. [h] Radiative decay rate constant, in 10^7 s^{-1}. [i] Nonradiative decay rate constant, in 10^9 s^{-1}. [j] Maximal phosphorescence emission wavelength in MeTHF, in nm, at 77 K. [k] Phosphorescence lifetimes at 610 nm ($\lambda_{ex} = 370$ nm), and $c = 1.0 \times 10^{-4}$ M, in ms, at 77 K. [l] CS quantum yields, in %. [m] Not applicable. [n] Literature values, ref. 25. [o] Not observed. [p] In ACN.

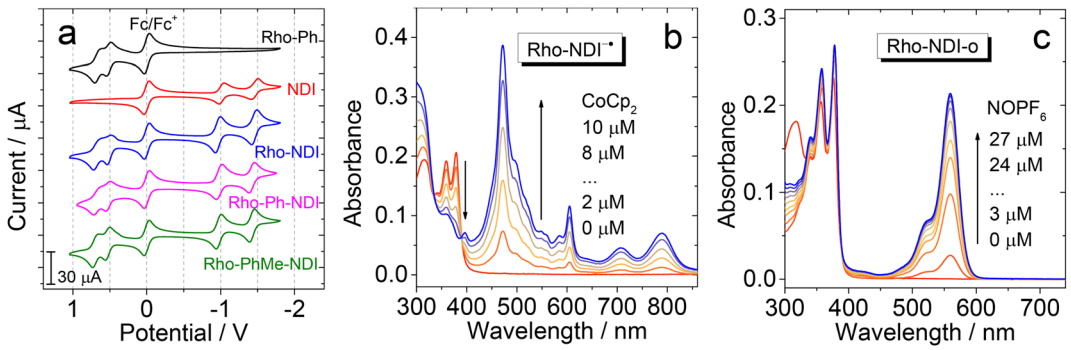

Fig. 4 (a) Cyclic voltammograms of the compounds in deaerated ACN. Ferrocene (Fc/Fc^+) was used as the internal reference (set as 0 V in the cyclic voltammograms). Conditions: in deaerated solvents containing 0.10 M $Bu_4N[PF_6]$ as the supporting electrolyte, and $Ag/AgNO_3$ as the reference electrode. Scan rate: 100 mV s^{-1} and $c = 1.0 \times 10^{-3}$ M. UV-vis absorption spectra of **Rho-NDI** (b) chemically reduced with $CoCp_2$ used to generate $NDI^{-\bullet}$ in deaerated DMF and (c) chemically oxidized with $NOPF_6$ in deaerated ACN. In this case the opened form of the dyad is produced. $c = 1.0 \times 10^{-5}$ M. 25 °C.

For **Rho-Ph-NDI** and **Rho-PhMe-NDI**, with a large separation distance between the donor and acceptor, in HEX and TOL, eqn (2) does not give correct values for ΔG_S because it overestimates the polarity of HEX and TOL. Therefore, we have used tentatively the value of $\Delta G_S = 0.56$ eV in HEX and $\Delta G_S = 0.4$ eV in TOL.[59] The CS state energy (E_{CSS}) in HEX (2.06 eV) obtained by this approximation also matches the energy obtained from the CS emission (Fig. 3a, 2.03 eV, estimated by 00 transition of $^1CS \rightarrow S_0$). For **Rho-NDI**, with a short separation distance between the donor and acceptor, the degree of overestimation for ΔG_S from eqn (2) in HEX (0.19) and TOL (0.13) is negligible. The results (Table 2) show that the CS is thermodynamically allowed for all the dyads. The driving force for the CS of **Rho-NDI** is larger than that of the dyads with a large separation distance

Table 2 Electrochemical redox potentials, Gibbs free energy changes of the charge separation (ΔG^0_{CS}) and the energy of the charge separated state (E_{CSS}) of the compounds in different solvents[a]

	E_{OX} (V)	E_{RED} (V)	ΔG^0_{CS} (eV)/E_{CSS} (eV) HEX	TOL	THF	ACN
NDI	—[b]	−1.02, −1.46	—[c]	—[c]	—[c]	—[c]
Rho-Ph	+0.52, +0.66	—[b]	—[c]	—[c]	—[c]	—[c]
Rho-NDI	+0.51, +0.67	−0.96, −1.45	−1.62/1.66	−1.68/1.60	−1.82/1.46	−1.87/1.41
Rho-Ph-NDI	+0.52, +0.66	−0.98, −1.42	−1.22/2.06	−1.38/1.90	−1.66/1.62	−1.82/1.46
Rho-PhMe-NDI	+0.53, +0.69	−0.97, −1.42	−1.22/2.06	−1.38/1.90	−1.66/1.62	−1.82/1.46

[a] Cyclic voltammetry in N_2-saturated solvents containing 0.10 M $Bu_4N[PF_6]$. Pt electrode as the counter electrode, glassy carbon as the electrode working electrode, ferrocene (Fc/Fc^+) as the internal reference (set as 0 V in the cyclic voltammograms), and $Ag/AgNO_3$ couple as the reference electrode in dichloromethane. $E_{00} = 3.28$ eV for **Rho-NDI**, **Rho-Ph-NDI** and **Rho-PhMe-NDI**. E_{00} is the approximated energy with the cross point of UV-vis absorption and fluorescence emission of **NDI** after normalization in HEX. For **Rho-Ph-NDI** and **Rho-PhMe-NDI**, in HEX, $\Delta G_S = 0.56$ eV is used; in TOL, $\Delta G_S = 0.40$ eV is used. THF stands for tetrahydrofuran. [b] Not observed. [c] Not applicable.

between the donor and acceptor (*i.e.* **Rho-Ph-NDI** and **Rho-PhMe-NDI**). The CS state energy (E_{CSS}) was calculated with eqn (5). The results show that for **Rho-NDI**, the CS state energy is <2.0 eV, which means that the low-lying triplet state is a CS state, not a ^{3}NDI* state, supported by nanosecond transient absorption (ns-TA) spectral studies (see the later section). For **Rho-Ph-NDI** and **Rho-PhMe-NDI**, the CS state energy is slightly higher than that of **Rho-NDI** in the same solvents. Thus, for these two dyads, the low-lying triplet state may probably be ^{3}NDI* in HEX, but in polar solvents, the CS state may become lower in energy. These postulates were confirmed by ns-TA spectral studies (see the later section).

$$\Delta G_S = -\frac{e^2}{4\pi\varepsilon_S R_{CC}} - \frac{e^2}{8\pi\varepsilon_0}\left(\frac{1}{R_D}+\frac{1}{R_A}\right)\left(\frac{1}{\varepsilon_{REF}}-\frac{1}{\varepsilon_S}\right) \quad (2)$$

$$\Delta G^0_{CS} = e[E_{OX} - E_{RED}] - E_{00} + \Delta G_S \quad (3)$$

$$\Delta G^0_{CR} = -(\Delta G^0_{CS} + E_{00}) \quad (4)$$

$$E_{CSS} = e[E_{OX} - E_{RED}] + \Delta G_S \quad (5)$$

In order to facilitate the assignment of the CS state in the transient absorption spectra, the UV-vis absorption of the radical anion and radical cation forms of the dyads was studied, with either a chemical reduction or spectroelectrochemistry method (Fig. 4b and c). For **Rho-NDI**, upon reduction with cobaltocene ($CoCp_2$), the absorption band centered at 375 nm is diminished, and new stronger absorption bands centered at 470 nm, 605 nm 707 nm and 790 nm emerge, which are attributed to the $NDI^{-\bullet}$ species (Fig. 4b).[60] These results are in agreement with the spectroelectrochemical studies (Fig. S25†). Similar results were observed for **Rho-Ph-NDI** and **Rho-PhMe-NDI** (Fig. S21†). The UV-vis spectra of $NDI^{-\bullet}$ for **Rho-NDI** were also recorded by the TDDFT method (Fig. S51†), which support the experimental results. With the oxidant of nitrosonium hexafluorophosphate ($NOPF_6$) added, intensive absorption bands centered at 520 nm and 560 nm appeared for **Rho-NDI** (Fig. 4c). These bands disappeared with the addition of TEA, which indicates that the new bands are attributed to the opened form of the Rho unit (**Rho-NDI-o**), not the radical cation of the Rho unit (Fig. S22†), although it is similar to the UV-vis spectra $Rho^{+\bullet}$ of **Rho-NDI** calculated by the TDDFT method. This information is useful for the study of the femtosecond transient absorption (fs-TA) and the ns-TA spectra of the compounds, for instance the identification of the transient species observed with these spectroscopic methods, especially the CS state.

Femtosecond transient absorption (fs-TA) spectroscopy

To verify the photophysical processes involved in the dyads upon photoexcitation, the fs-TA spectra of the dyads were recorded. For **NDI**, the result of a target analysis of the fs-TA data with a scheme including S_1/T_n state equilibrium is shown in Fig. S26.† The S_1 state with an absorption band centered at 597 nm was populated after photoexcitation. Then the fast ISC process $S_1 \rightarrow T_n$ (absorption at 467 nm) occurs (*via* spin orbit coupling ISC, SOC-ISC), and the T_n state has a lifetime of 2.6 ps, due to the similar energy of the two states of S_1 (3.26 eV, based on the spectroscopic data) and T_n (3.24 eV, based on the DFT calculation). The reverse ISC of the T_n state to the S_1 state (4.3 ps) competes with internal conversion to lower triplet states T_1 (6.3 ps). The T_1 state does not decay completely within the available time window of the fs-TA spectrometer, which is supported by the ns-TA spectra.[61]

The fs-TA spectra of **Rho-NDI** and **Rho-Ph-NDI** in different solvents upon fs laser excitation at 375 nm are shown in Fig. 5. The species-associated difference spectra (SADS) of the dyads were obtained by global fitting with the sequential model. For **Rho-NDI**, two species were required for the satisfactory fitting of the spectra in HEX (Fig. 5b). The ground state bleaching (GSB) band was observed in the range of 330–400 nm, which is in agreement with the steady-state absorption spectrum (Fig. 2). The first species is assigned to the mixed state of S_1 and a higher triplet state (T_n), showing excited state absorption (ESA) bands centered at 593 nm (S_1) and 468 nm (T_n). ISC (<120 fs, response function time of the instrument) is too fast for the S_1 and a higher triplet T_n state with similar energy to be isolated as two species from the fs-TA spectra. After 285 fs, the second species is formed, showing the typical absorption of $NDI^{-\bullet}$ centered at 475 nm and 607 nm. Thus, the process upon photo-excitation can be summarized as ^{1}NDI* $\rightarrow$ ^{3}NDI* (an upper triplet state) $\rightarrow$ ^{3}CS or ^{1}NDI* $\rightarrow$ ^{1}CS. Concerning the low charge separation efficiency of the ^{3}CS (10–25%, see the later ns-TA section) for the dyads, the main pathway may be ^{1}NDI* $\rightarrow$ ^{1}CS, followed by ^{1}CS $\rightarrow$ S_0, which competes with the process of ^{1}CS $\rightarrow$ ^{3}CS. The lifetime of the CS state in fs TA spectra is determined to be 210 ps, although the signal can be observed in a longer time window (see the ns-TA section), which is likely due to the lower spectral resolution of the fs-TA spectrograph and a lower signal-to-noise ratio of the setup employed. In ACN, a similar EADS result was observed, CS (*i.e.*, the lifetime of the first species) was determined to be 160 fs, and the CS state lifetime was 1.4 ps (Fig. 5c).

For **Rho-Ph-NDI** and **Rho-PhMe-NDI**, similar fs-TA spectra and SADS fitting results were observed (Fig. 5d–f and S26†) in both HEX and ACN. An upper excited triplet state, for which the energy is close to that of the S_1 state, was generated by fast ISC (<120 fs). Then the CS process occurs to generate the CS state. Based on the electrochemical studies and DFT results, For **Rho-Ph-NDI** and **Rho-PhMe-NDI**, the low-lying triplet state is a LE state in HEX, and thus, we assume that ^{3}NDI* was generated by the CR process from the CS state. The ^{3}NDI* state was not obtained in fs-TA spectra, probably due to the slow CR process.

Nanosecond transient absorption (ns-TA) spectroscopy

In order to study the long-lived species of the dyads formed upon photoexcitation, the ns-TA spectra of the compounds were recorded (Fig. 6). For **Rho-NDI**, a positive absorption band centered at 470 nm and a minor absorption band centered at 600 nm were observed upon nanosecond pulsed laser excitation (Fig. 6a). These absorption bands are attributed to $NDI^{-\bullet}$, based on the chemical reduction results (Fig. 4). The weak absorption of $Rho^{+\bullet}$ may be overshadowed by the strong absorption of $NDI^{-\bullet}$.

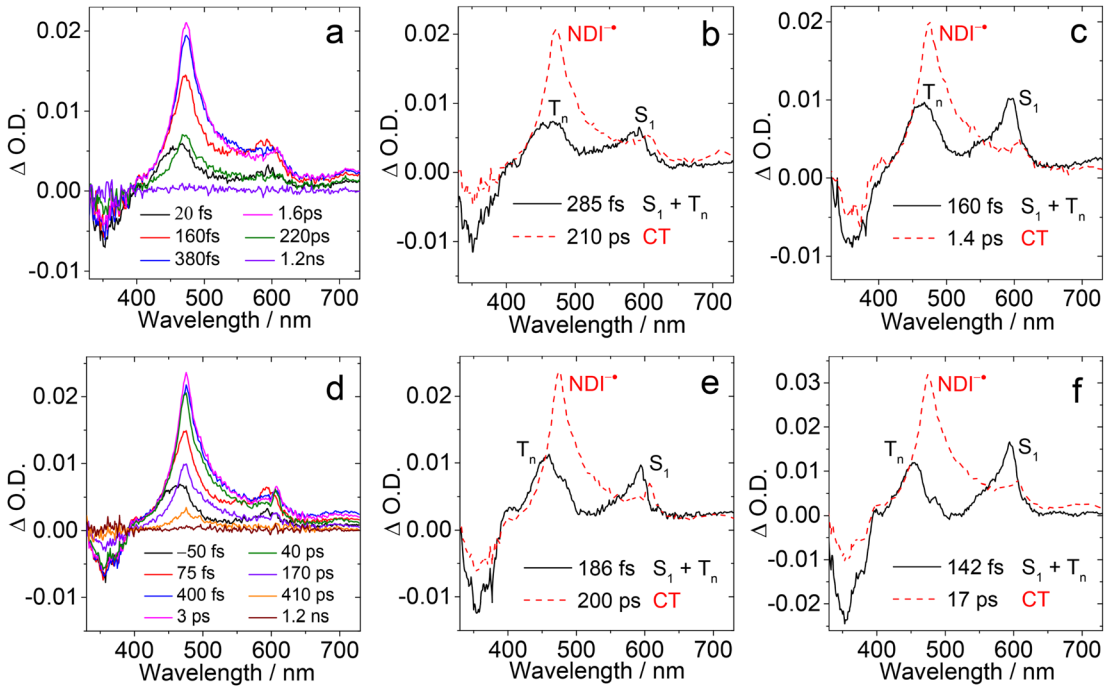

Fig. 5 Femtosecond transient absorption spectra of (a) **Rho-NDI** and (d) **Rho-Ph-NDI** in HEX. The related species-associated difference spectrum (SADS) obtained from target analysis with the sequential model in (b) HEX and (c) ACN for **Rho-NDI**, and (e) HEX and (f) ACN for **Rho-Ph-NDI** is presented. $\lambda_{ex} = 375$ nm. $c = 1.0 \times 10^{-4}$ M, and 25 °C.

The decay of the transient species has a biexponential feature (Fig. 6b), and the shorter component has a lifetime of 0.13 μs (population rate 93.5%), and a longer component of 4.0 μs (6.5%). Based on the CS emission lifetime (0.09 ns (91.2%)/ 2.91 ns (8.8%), Fig. S20†), the first component is attributed to the ^{3}CS state, not the ^{1}CS state. The second component is attributed to intermolecular CR (see the later section). We recorded the ns-TA spectra of **Rho-NDI** in deaerated viscous solvent dimethyl silicone oil 500 (a solvent with low-polarity). Diffusion based photophysical processes, such as triplet–

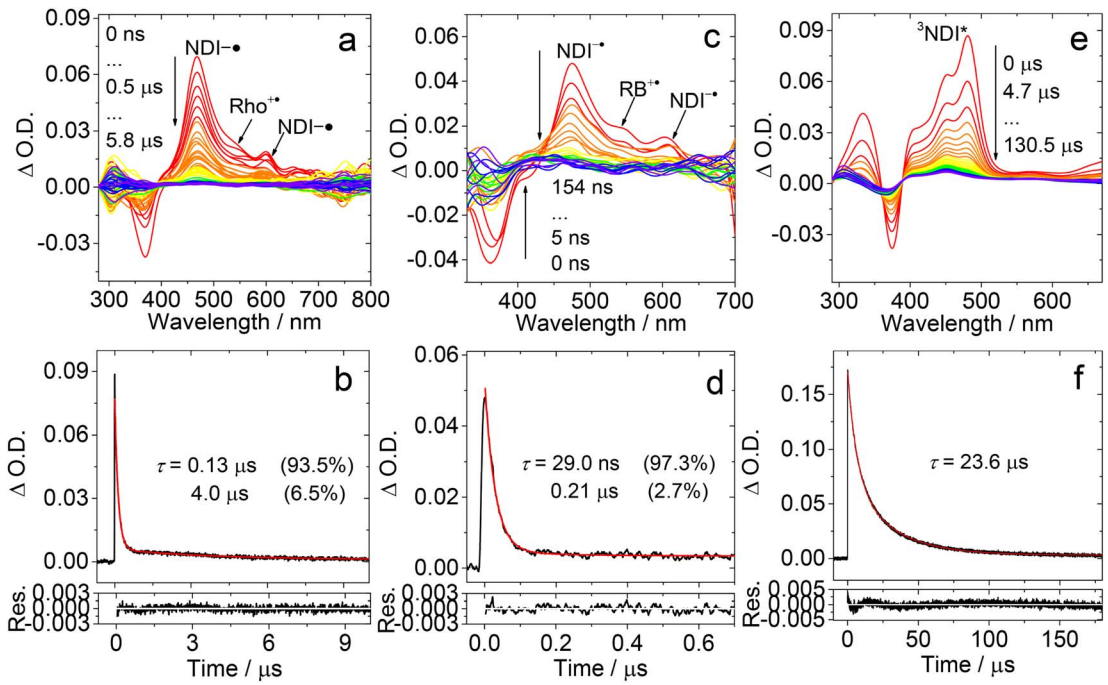

Fig. 6 Nanosecond transient absorption spectra of **Rho-NDI** in deaerated (a) HEX and (c) ACN. The decay traces of **Rho-NDI** in deaerated (b) HEX at 480 nm and (d) ACN at 470 nm, excited with a nanosecond pulsed laser. (e) Nanosecond transient absorption spectra of **NDI** and (f) the decay trace of **NDI** at 485 nm in deaerated HEX excited with a nanosecond pulsed laser. $\lambda_{ex} = 355$ nm. $c = 3.0 \times 10^{-5}$ M, and 25 °C.

triplet annihilation or intermolecular electron transfer, should be inhibited in viscous solvent. Mono-exponential decay $NDI^{-\bullet}$ of **Rho-NDI** was observed and the lifetime was determined to be 151.5 ns (Fig. S37†), which indicates that the second component of the decay traces of **Rho-NDI** in deaerated HEX and ACN (Fig. 6) is due to the intermolecular CR process. This is a long-lived CS state, considering that **Rho-NDI** is a compact dyad.[35] Previously for a ZnPor-C_{60} dyad, the CS state lifetime was determined to be 530 ns.[18]

In polar solvent ACN, similar ns-TA spectra were obtained, but the lifetime of the first component was shortened to *ca.* 29 ns and the lifetime of the second component was reduced to 0.21 μs (Fig. 6c and d). In aerated HEX, the monoexponential decay $NDI^{-\bullet}$ of **Rho-NDI** was observed and the lifetime was quenched to 91.1 ns (Fig. S31†).

These results show that the transient species are most likely in triplet spin multiplicity, *i.e.* the ^{3}CS state was detected, not the ^{1}CS state. Similarly, the lifetime of $NDI^{-\bullet}$ was quenched to 20.8 ns with monoexponential decay in aerated ACN (Fig. S31†). In deaerated TOL, the signal of $NDI^{-\bullet}$ is very weak with a lifetime of 0.39 μs (Fig. S30†), which is longer than that in HEX and ACN. The abnormal long-lived $NDI^{-\bullet}$ is due to the intermolecular CT resulting from the high concentration of measurement.

We also recorded the ns-TA spectra of the reference compound **NDI** under similar conditions (Fig. 6e). A positive absorption band is located in the region <500 nm, which is attributed to the ^{3}NDI* absorption ($T_1 \rightarrow T_n$ transition). Moreover, the NDI* state lifetime was determined to be 23.6 μs (Fig. 6f). These results corroborate the assignment of the CS state in the ns-TA spectra of **Rho-NDI**. These results infer that the CS state has a lower energy than the ^{3}NDI* state in **Rho-NDI**, which is in agreement with the electrochemical studies (Table 2).

The Φ_{CS} was determined using the relative method (eqn (S1)†). The molar absorption coefficient of $NDI^{-\bullet}$ ($\varepsilon_{475\ nm} = 38\ 700\ M^{-1}\ cm^{-1}$) was determined by the chemical reduction method and is similar to the reported value ($\varepsilon_{475\ nm} = 40\ 000\ M^{-1}\ cm^{-1}$).[46] The molar absorption coefficient of $Rho^{+\bullet}$ was determined to be *ca.* 6600 $M^{-1}\ cm^{-1}$ at 560 nm by spectroelectrochemistry. The strong absorption of the T_1 state of anthracene ($\varepsilon_{432\ nm} = 45\ 500\ M^{-1}\ cm^{-1}$; $\Phi_T = 0.71$) was used as a standard to obtain the Φ_{CS}, based on the absorption of $NDI^{-\bullet}$.[62,63] The Φ_{CS} of **Rho-NDI** in HEX was determined to be 25% (Fig. S49†). It should be noted that the Φ_{CS} is attributed to the ^{3}CS state due to the long lifetime detected in ns-TA rather than total CS states (both ^{1}CS and ^{3}CS states).

The ns-TA spectra of **Rho-Ph-NDI** were studied (Fig. 7). With the intervening phenyl linker, we anticipate that the CS state energy should increase as compared to that of **Rho-NDI**.[31] In HEX, an intensive positive absorption band centered at 480 nm was observed, which is similar to that of **NDI**. Thus, it is attributed to the ESA band of the ^{3}NDI* state. The lifetime was determined to be 1.10 μs (Fig. 7a and b). For **Rho-Ph-NDI**, the CS state energy in HEX is 2.06 eV, which is slightly higher than that of ^{3}NDI* (2.04 eV), where they are in equilibrium. Therefore, for **Rho-Ph-NDI**, fast decay of ^{3}NDI* (1.10 μs) is observed, but it is much shorter than the triplet state lifetime of native **NDI** (23.6 μs, Fig. 6f).

The ns-TA spectra of **Rho-Ph-NDI** in TOL were also recorded (Fig. 7c), and interestingly, positive absorption bands centered at 477 nm and 610 nm were observed, and thus the transient species was assigned to the CS state. The CS state lifetime was determined to be 0.37 μs (58%)/5.8 μs (42%) (Fig. 7d), which is longer than that of **Rho-NDI** (0.13 μs. In HEX). Note that the CS state lifetime is much longer than the CS state fluorescence lifetime (0.32 ns (60.3%)/3.13 ns (39.7%), Fig. S20†), and thus we assign the CS state observed in the ns-TA spectra to the ^{3}CS state, not the emissive ^{1}CS state. This longer CS state lifetime may be due to the weaker electronic coupling, as a result of the intervening phenyl linker. In polar solvent ACN, similar ns-TA spectra were observed, and the lifetime of the CS state was determined to be 0.72 μs (90.6%)/512.8 μs (9.4%) (Fig. 7e and f), which is also much longer than that of **Rho-NDI** (29 ns).

To clarify the longer-lived component of the decay of the transient of **Rho-Ph-NDI** in TOL, the ns-TA spectra of **Rho-Ph-NDI** in deaerated viscous solvent dimethylsilicone oil 500 (relative dielectric constant $\varepsilon_r = 2.75$, for which the polarity is similar to that of TOL, $\varepsilon_r = 2.38$) were recorded (Fig. S37†). Biexponential decay $NDI^{-\bullet}$ of **Rho-Ph-NDI** was observed and the lifetime was determined to be 0.57 μs (88%)/7.4 μs (12%). Thus, the component with a longer lifetime is due to the close-lying CS state and the ^{3}NDI* state rather than the diffusion controlled intermolecular CR, which is different from **Rho-NDI**. This conclusion is supported by the similar energy of the CS state (1.90 eV) calculated by electrochemistry and the ^{3}NDI* state (2.04 eV, see the later section). In polar viscous solvent triacetin ($E_T(30) = 40.4$ kcal mol^{-1}), the CS state lifetime is 0.68 μs with monoexponential decay, which indicates that the second component of the fitting of the decay traces of **Rho-Ph-NDI** in ACN is attributed to the intermolecular charge recombination (Fig. S38†).

Rho-PhMe-NDI, with the attachment of methyl groups on the intervening phenyl linker, shows analogous spectra and triplet state lifetime compared with **Rho-Ph-NDI** (Fig. S34†). In HEX, the ^{3}NDI* state (2.0 μs) was observed, which is almost two times that of **Rho-Ph-NDI**. In TOL, the CS state lifetime was determined to be 0.63 μs (70.4%)/5.4 μs (29.6%). In ACN, the CS state lifetime is 0.59 μs (87.4%)/595.1 μs (12.6%) similar to that of **Rho-Ph-NDI**, which is much longer than that of **Rho-NDI**. We tentatively attribute this longer CS state lifetime to the weaker electronic coupling in **Rho-Ph-NDI** and **Rho-PhMe-NDI** than that in **Rho-NDI**, as a result of the longer linker in the former. For **Rho-Ph-NDI** and **Rho-PhMe-NDI**, the Φ_{CS} in TOL is low and determined to be 7% and 3%, respectively; the Φ_{CS} in ACN was determined to be 19% and 17%, respectively (Fig. S49†), which is slightly lower than that of **Rho-NDI** in HEX (25%).

Steady state and time-resolved electron paramagnetic resonance (TREPR) spectroscopy

EPR experiments were performed to obtain information on the spin density distribution within the anion radicals of the compounds (Fig. 8). The radical anions of the compounds were

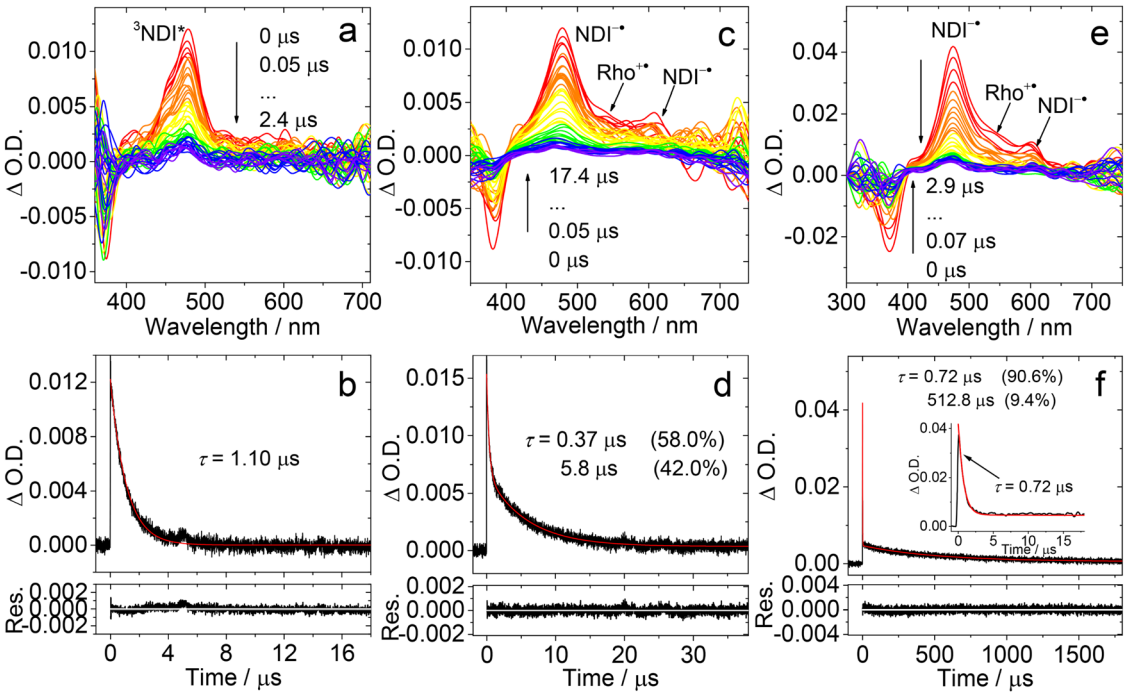

Fig. 7 Nanosecond transient absorption spectra of **Rho-Ph-NDI** in deaerated (a) HEX, (c) TOL and (e) ACN. The decay traces of **Rho-Ph-NDI** in deaerated (b) HEX at 485 nm, (d) TOL and (f) ACN at 470 nm. Excited with a nanosecond pulsed laser. $\lambda_{ex} = 355$ nm. $c = 3.0 \times 10^{-5}$ M in HEX, $c = 5.0 \times 10^{-5}$ M in TOL and ACN, and 25 °C.

prepared by chemical reduction with tetrabutylammonium fluoride (TBAF) in deaerated DMF.[64,65]

Since **NDI** is *N*,*N* symmetrically disubstituted, the hydrogen atoms located on the aromatic core exist in equivalent environments. The hyperfine coupling (HFC) constants of **NDI** obtained by simulation of the experimental EPR spectra show two equivalent nitrogen atoms (0.98 G) and four equivalent protons (1.86 G), which are close to the values obtained by DFT calculations at the UB3LYP/EPR-II level (Table S3†).[60,66] For **Rho-Ph-NDI** and **Rho-PhMe-NDI**, similar results and HFC constants observed as compared to **NDI**, which indicates that the electron donor Rho has negligible effect on the spin density distribution of NDI$^{-\bullet}$ due to the linkers (phenyl and *p*-xylene, respectively) between the Rho and **NDI** units. However, for **Rho-NDI**, two pairs of equivalent nitrogen atoms (1.03 G/0.97 G) and protons (1.98 G/1.82 G) are needed to simulate the EPR spectra, revealing that a weak coupling of the N atoms of the Rho and the **NDI** moiety is present due to the direct link of the donor and acceptor. The HFC constants of **Rho-NDI** calculated by DFT also provide evidence for the asymmetry of spin density distribution of NDI$^{-\bullet}$ (Table S3†).[46] These results verify the fact mentioned above that weaker electronic coupling exists in **Rho-Ph-NDI** and **Rho-PhMe-NDI** than that in **Rho-NDI**, as a result of the longer linker in the former two dyads. Despite the slight differences between the spectra of **Rho-NDI** and other dyads, as well as **NDI**, NDI$^{-\bullet}$ of the compounds has virtually identical *g* values (2.0044 for **NDI**, 2.0043 for **Rho-NDI**, 2.0046 for **Rho-Ph-NDI**, and 2.0040 for **Rho-PhMe-NDI**. Table 3). The isotropic hyperfine splitting parameters of NDI$^{-\bullet}$ of the compounds based on EPR spectra are summarized in Table 3. Based on the above results, we propose that the *J* and the electron spin–spin interaction of Rho$^{+\bullet}$-NDI$^{-\bullet}$ (*i.e.* CS state) are stronger than those of **Rho-Ph-NDI** and **Rho-PhMe-NDI.**

In order to understand the nature of the photoexcited states, we performed a series of time-resolved electron paramagnetic resonance (TREPR) spectroscopy measurements as shown in Fig. 9. All spectra were recorded in frozen solution at 80 K; the spectra recorded at higher temperatures (185 and 285 K, Fig. S53†) feature complex dynamics and will not be discussed in detail. Fig. 9 clearly shows that the spectra of **Rho-NDI**, **Rho-Ph-NDI** and **Rho-PhMe-NDI** consist of two overlapping signals:

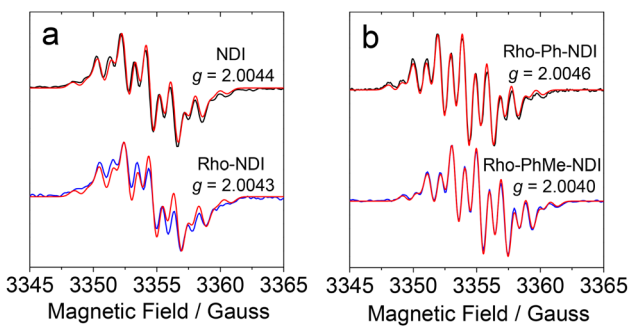

Fig. 8 EPR spectra of NDI$^{-\bullet}$ of (a) **NDI** and **Rho-NDI** and (b) **Rho-Ph-NDI** and **Rho-PhMe-NDI**, generated by TBAF in deaerated DMF and corresponding *g* values. The red lines in the spectra are the simulation results. *c*[Sample] = 1.0×10^{-4} M, *c*[TBAF] = 0.05 M, and 25 °C. Microwave frequency = 9.41 GHz, microwave power = 0.796 mW, and modulation amplitude = 1 G.

a dominant broader signal similar to the TREPR spectrum of the triplet state of **NDI** (see also Table 4) and a narrow weak signal in the center of the spectrum, most likely originating from a ^{3}CS state, which can be described as a spin-correlated radical pair (SCRP).

Broad dominant signals shown in Fig. 9a are assigned to NDI-localized triplets formed *via* common SOC-ISC, because the native **NDI** gives the same signal. Subtle differences in the simulation parameters (Table 4) obtained for dyads and individual **NDI** can be attributed to the minor structural influence on a spin density distribution. The differences of this kind, *e.g.*, in *D*-tensor parameters between a triplet of a pristine compound based on SOC-ISC and a triplet localized on it in a dyad based on SOCT-ISC have been reported previously.[67–69]

In principle, the weak and narrower signals shown in Fig. 9b can be assigned either to CS states [$D^{+\bullet}$–$A^{-\bullet}$] or to highly delocalized triplet states ^{3}[D–A*] of the dyads. Narrow widths of the spectra infer that the two electrons are weakly coupled, *i.e.* both the zero-field splitting value and dipolar splitting are relatively small; therefore, the presence of a SCRP [$D^{+\bullet}$–$A^{-\bullet}$] is more likely.

Generally, a triplet state can be formed *via* common SOC-ISC, *via* SOCT-ISC, or *via* a radical pair ISC (RP-ISC). RP-ISC can provide an asymmetric polarization pattern in some cases,[70,71] whereas SOC/SOCT-ISC always results in a symmetric one (assuming no anisotropic relaxation). None of these mechanisms alone can describe the patterns observed for dyads, *e.g.* asymmetric narrow signal with polarization type *ea* (*e* stands for emission and *a* – for absorption) for **Rho-Ph-NDI** (Fig. 9).

The signal originating from a charge-separated state has distinctive features given by weak spin coupling in its Hamiltonian and a resulting mixing of $|S\rangle$ and $|T_0\rangle$ levels.[31,32,72,73] Taking into account a dipolar interaction, both these factors provide a specific orientation dependence of a spectrum. To simulate such a spectral shape, we used a routine based on some functions of the EasySpin package for MatLab (note that exchange interaction in EasySpin is introduced within a spin Hamiltonian $\hat{H}_{ex} = J\vec{S_1}\vec{S_2}$, whereas ref. 51 and 52 use $\hat{H}_{ex} = -2J\vec{S_1}\vec{S_2}$).[74]

The results of the simulations are given in Table 5. We used closely isotropic $\hat{g}$-tensors ≈2.003; hyperfine interaction was neglected. $|D|$ in Table 5 stands for the absolute value of dipole interaction and it is consistent with the structures shown in Fig. 9, where **Rho-NDI** has the smallest distance between Rho and **NDI** moieties. Consequently, **Rho-NDI** must feature the largest value of dipolar interaction ($|D|$ = 184 MHz) compared with **Rho-Ph-NDI** ($|D|$ = 39 MHz) and **Rho-PhMe-NDI** ($|D|$ = 41 MHz), and the assumption is consistent with the simulation result. Moreover, the

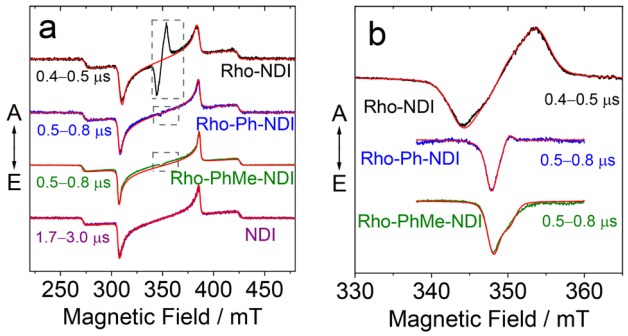

Fig. 9 TREPR spectra of (a) the studied compounds and (b) magnified narrow central-field range (baseline corrected). Simulation curves are shown in red, and experimental results in other colors. The spectra were obtained under 355 nm laser irradiation at 80 K in glassy TOL. The spectra correspond to the integrals over time windows after the laser flash indicated in the figure (the maximum of TREPR signal kinetics).

$|D|$-values of the three dyads differ by a factor of ~4–5, in agreement with estimations based on optimized ground state structures and point-dipole approximation.

Thus, we succeeded to simulate weak features in the center of the spectra of all three dyads in a model of a CS state (SCRP) with weak electronic couplings. At the same time, we note that these features of **Rho-NDI** and **Rho-PhMe-NDI** can also be simulated as a superposition of two delocalized ^{3}[D–A*] triplets: SOC-ISC triplet and RP-ISC triplet.[70,71] However, in the case of **Rho-Ph-NDI** only the SCRP model provides satisfactory agreement. Therefore, most likely, we deal with CS states in the whole series of dyads, although for **Rho-NDI** and **Rho-PhMe-NDI** it cannot be proven by TREPR alone. Moreover, for the CS state of **Rho-NDI**, the *e*,*a* → *a*,*e* phase change of the CS state spectrum with increasing the delay time (Fig. S50 and S52†) is observed, which likely originates from the repopulation of the CS state from a singlet to a triplet state, *i.e.* the process ^{1}NDI* → ^{1}[$Rho^{+\bullet}$–$NDI^{-\bullet}$] → ^{3}[$Rho^{+\bullet}$–$NDI^{-\bullet}$] in addition to ^{3}NDI* → ^{3}[$Rho^{+\bullet}$–$NDI^{-\bullet}$],[75,76] which further supports that the long-lived CS state is due to the electron spin control effect. Similar phase change behaviors were observed for **Rho-Ph-NDI** and **Rho-PhMe-NDI** (*e*,*a* → *a*,*e* and *e* → *a*, correspondingly), although the TREPR signal of the CS state is weak (Fig. S50†). The spectral shapes of the observed CS state are determined by an interplay of *D* and *J* values, and only for **Rho-NDI** each of them can be reliably obtained (Table 5). In the cases of **Rho-Ph-NDI** and **Rho-PhMe-NDI** both $|D|$ and $|J|$ are rather small; however, their range agrees well with literature data in similar situations.[19,25,28,31,77]

Table 3 Isotropic hyperfine splitting parameters for the EPR spectra of $NDI^{-\bullet}$ for the compounds[a]

		NDI	Rho-NDI	Rho-Ph-NDI	Rho-PhMe-NDI
g		2.0044	2.0043	2.0046	2.0040
α/G[b]	^{14}N (n[c])	0.98 (2)	1.03 (1)/0.97 (1)	0.98 (2)	0.98 (2)
	^{1}H (n[c])	1.86 (4)	1.98 (2)/1.82 (2)	1.88 (4)	1.88 (4)
Linewidth/G		0.103	0.105	0.090	0.094

[a] $NDI^{-\bullet}$ of the compounds was generated by TBAF in deaerated DMF. *c*[Sample] = 1.0×10^{-4} M, *c*[TBAF] = 0.05 M, and 25 °C. Microwave frequency = 9.41 GHz, microwave power = 0.796 mW, and modulation amplitude = 1 G. [b] HFC constants. [c] The number of equivalent atoms.

Table 4 The simulation parameters of the SOC-ISC triplet state localized on the NDI moiety for dyads and pristine NDI. Zero-field splitting (ZFS) parameters ($|D|$ and $|E|$), relative population rates P_x, P_y, and P_z of the zero-field spin states, and the unique ratio of populations $\Delta P = |P_x - P_y|/|P_y - P_z|$ of the triplet state of the compounds

Compounds	$\|D\|$ (MHz)	$\|E\|$ (MHz)	$P_x : P_y : P_z$	ΔP
NDI	2121	34	0.46 : 1 : 0	0.54
Rho-NDI	2075	34	0.76 : 1 : 0	0.24
Rho-Ph-NDI	2115	29	0.51 : 1 : 0	0.49
Rho-PhMe-NDI	2144	30	0.35 : 1 : 0	0.65

Table 5 The simulation parameters for the studied dyads. J is the exchange coupling taken in the form $\hat{H}_{ex} = J\overrightarrow{S_1}\overrightarrow{S_2}$. $|D|$ is the scalar parameter of zero-field splitting ($|E| = 0$). P_{-1}, P_0, P_{+1}, and P_s are the representative populations of $|T_{-1}\rangle$, $|T_0\rangle$, $|T_{+1}\rangle$, and $|S\rangle$ states, correspondingly

Compounds	$\|J\|$/MHz	$\|D\|$/MHz	$P_{-1} : P_0 : P_{+1} : P_s$
Rho-NDI	26	184	0.92 : 1 : 0.92 : 0
Rho-Ph-NDI	23	39	0.98 : 1 : 0.90 : 0
Rho-PhMe-NDI	28	41	0.80 : 1 : 0 : 0

Finally, it should be pointed out that TREPR spectral kinetics shows that the decay of the "minor feature" (Fig. S50†), associated with the CS state $^3[D^{+\bullet}\text{–}A^{-\bullet}]$, is an order of magnitude (~5–20 times) shorter than that of the NDI-localized SOC triplet (broad dominant component of the TREPR spectra). This fast decay of polarization makes the TREPR signal of this feature much weaker compared to the dominant signal; in addition, we note that the polarization formed by different mechanisms can differ strongly in intensity. Moreover, it is noteworthy that the spectra of spin-correlated radical pairs are the result of the mutual cancelling of an absorptive and an emissive signal if $|J|$ and $|D|$ both are relatively small.[78] This is exactly the case for **Rho-Ph-NDI** and **Rho-PhMe-NDI**; therefore, the minor $^3[D^{+\bullet}\text{–}A^{-\bullet}]$ signal of the **Rho-NDI** spectrum is much more intensive compared to $^3[D^{+\bullet}\text{–}A^{-\bullet}]$ signals in **Rho-Ph-NDI** and **Rho-PhMe-NDI**. Saying that, we stress that the weak intensity of the $^3[D^{+\bullet}\text{–}A^{-\bullet}]$ TREPR signal compared to the NDI-localized signal should not necessarily be interpreted as a small contribution of the former pathway compared to the latter one.

Theoretical computations

The ground state geometry of the compounds was optimized by DFT calculations (Fig. 10). For **Rho-NDI**, the dihedral angle between the π-conjugation planes of the xanthene moiety and **NDI** is 63.6°, which is slightly different from the molecular structure determined by the single crystal X-ray diffraction experiments (52.9°), and the difference probably results from the packing effect in the single crystal. The corresponding dihedral angles of **Rho-Ph-NDI** and **Rho-PhMe-NDI** between the xanthene and the **NDI** moieties are 86.3° and 76.9°, respectively, larger than that of **Rho-NDI**. For **Rho-Ph-NDI**, the dihedral angle of the xanthene moiety and the phenyl is 83.1°, and the dihedral angle between the phenyl and **NDI** moieties is 89.1°, which are all lager than that of **Rho-PhMe-NDI** (64.0° for xanthene and *p*-xylene and 79.0° for *p*-xylene and **NDI**, respectively). The centroid-to-centroid distances between the xanthene and the **NDI** moieties are 6.0 Å, 10.1 Å, and 9.9 Å, in **Rho-NDI**, **Rho-Ph-NDI** and **Rho-PhMe-NDI**, respectively.

The frontier molecular orbitals (MOs) are presented in Fig. 11a. For the dyads, the highest occupied molecular orbital (HOMO) is localized on the Rho moiety and the lowest unoccupied molecular orbital (LUMO) is localized on the **NDI** moiety. There is negligible delocalization on two moieties for both MOs.

The electron spin density surfaces of the T_1 state of the dyads in different polarity solvents were also studied (Fig. 11b). For **Rho-NDI**, the electron spin density of the T_1 state is delocalized on the whole molecule in both TOL and ACN. These results are in agreement with the ns-TA spectral results that a CS state was observed for **Rho-NDI**. For **Rho-Ph-NDI**, the spin density of the T_1 state is localized on the **NDI** moiety in low-polarity solvent HEX, but it is delocalized on the whole molecule in TOL and ACN, which is in agreement with the observation that the ^{3}NDI state in HEX but a CS state was observed in TOL and ACN (Fig. 7). For **Rho-PhMe-NDI**, the spin density distribution was similar to that of **Rho-Ph-NDI** in HEX and ACN, which is also in accordance with the result of the ns-TA spectra.

Based on the above results, the energy diagrams of the dyads were constructed as shown in Schemes 2 and S1.† Upon photoexcitation of the **NDI** moiety, the singlet excited state of the dyads was populated. Then, fast ISC (<120 fs) produces an upper triplet state (T_n, whose energy approximately is equal to the energy of ^{1}NDI*).

The CT process takes 186 fs for **Rho-Ph-NDI** and 175 fs for **Rho-PhMe-NDI** to generate the CS state. Concerning the low Φ_{CS} of the triplet CS state (17–25%) for the dyads, the major pathway is CT from ^{1}NDI* to generate the ^{1}CS state, taking 285 fs. Subsequently, the process of $^1\text{CS} \rightarrow S_0$ competes with ISC from the ^{1}CS state to the ^{3}CS state to generate a long-lived ^{3}CS state (0.13 μs in HEX for **Rho-NDI**). For **Rho-Ph-NDI**, the ^{3}NDI* state with a lifetime of 1.1 μs was produced by CR in low-polarity solvent HEX due to the low-

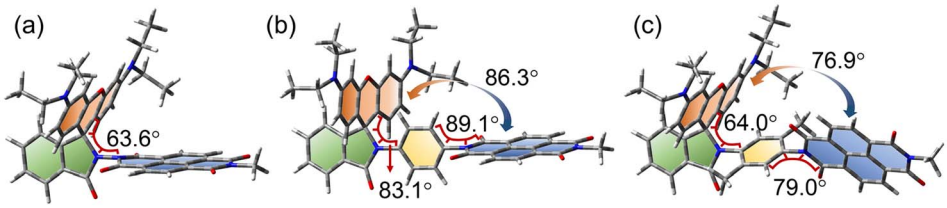

Fig. 10 Optimized ground state geometry of (a) **Rho-NDI**, (b) **Rho-Ph-NDI**, and (c) **Rho-PhMe-NDI**. The selected dihedral angles are presented. Calculations were performed by DFT at the B3LYP/6-31G(d) level with Gaussian 09.

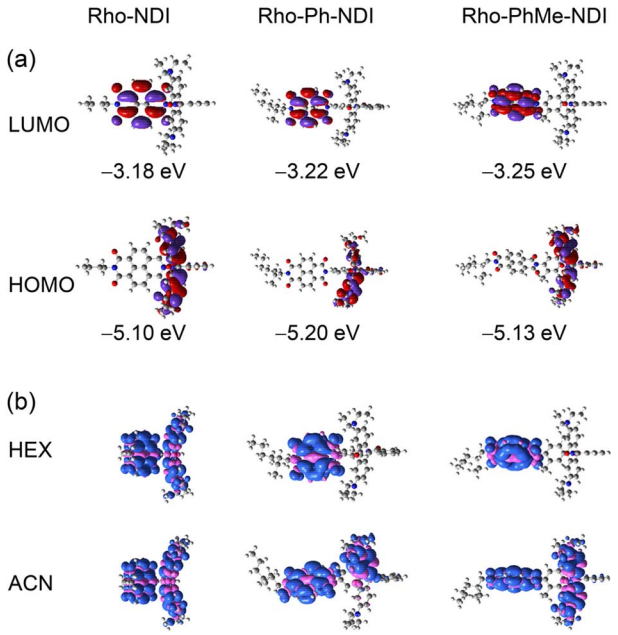

Fig. 11 (a) Selected frontier molecular orbitals of the dyads calculated by DFT at the B3LYP/6-31G(d) level with Gaussian 09 (isovalue = 0.02). The energy of the orbits is presented (in eV). (b) Isosurfaces of spin density at the optimized triplet state geometries of the dyads in HEX and ACN. Calculation was performed by DFT at the CAM-B3LYP/6-31G(d) level with Gaussian 09 (isovalue = 0.0004).

lying ^{3}NDI* state, and the long-lived ^{3}CS state was generated in TOL (0.37 μs (58%)/5.8 μs (42%)) and ACN (0.72 μs). For **Rho-PhMe-NDI**, a photophysical process similar to that of **Rho-Ph-NDI** was observed upon photoexcitation. In HEX, the CR process gives the ^{3}LE state localized on the **NDI** moiety (2.0 μs). The ^{3}CS state was produced with a lifetime of 0.63 μs (70%)/5.4 μs (30%) in TOL and 0.59 μs in ACN. For all dyads, a CS state with a long lifetime was generated by the electron spin control effect. Compared with **Rho-NDI**, the phenyl and *p*-xylene linkers of **Rho-Ph-NDI** and **Rho-PhMe-NDI**, leading to the weaker electronic coupling between the donor and acceptor, prolong the CS state lifetime.

Conclusions

In summary, we prepared three spiro electron donor–acceptor dyads, with the closed form of rhodamine (Rho) as the electron donor and naphthalenediimide (**NDI**) as the electron acceptor, to access the long-lived triplet charge separation (^{3}CS) state based on the electron spin control effect. The distance and electronic coupling between the donor and acceptor are regulated by direct connection of Rho and **NDI** units for **Rho-NDI** or *via* an intervening phenyl or *p*-xylene linker between Rho and **NDI** units (**Rho-Ph-NDI** and **Rho-PhMe-NDI**, respectively). The dihedral angle (based on the optimized ground state geometry) between the xanthene and the **NDI** moieties is 63.6°, 86.3° and 76.9°, respectively. Compared to **Rho-NDI**, the longer distance between Rho and **NDI** moieties results in weaker electronic coupling for **Rho-Ph-NDI** and **Rho-PhMe-NDI**. Femtosecond transient absorption (fs-TA) spectra indicated that for all dyads fast ISC of the **NDI** unit takes less than 120 fs upon photoexcitation, and then charge separation (CS) from an upper ^{1}NDI* and ^{3}NDI* state takes hundreds of fs to generate the CS state. Nanosecond transient absorption (ns-TA) spectra show the formation of the ^{3}CS state of **Rho-NDI** in different polarity solvents *n*-hexane (HEX), toluene (TOL) and acetonitrile (ACN). In HEX, the CS state lifetime is 0.13 μs, and the CS quantum yield (Φ_{CS}) of the ^{3}CS state is 25%. For **Rho-Ph-NDI** and **Rho-PhMe-NDI**, a triplet state localized on the **NDI** moiety (^{3}NDI*) was observed in HEX, whereas long-lived CS states with a lifetime of 0.37 μs (58%)/5.8 μs (42%) for **Rho-Ph-NDI** and 0.63 μs (70.4%)/5.4 μs (29.6%) for **Rho-PhMe-NDI** were observed in TOL. The Φ_{CS} of **Rho-Ph-NDI** was 19% and that of **Rho-PhMe-NDI** was 17%. The long-lived CS state of the dyads is based on the electron spin control effect, that is, to generate the final CS state with a triplet precursor (^{3}NDI* state). With electron paramagnetic resonance (EPR) spectra, we prove the weak yet non-negligible electronic coupling between the Rho and **NDI** moieties for **Rho-NDI**. Time-resolved EPR (TREPR) spectra show that two transient species exist for the dyads upon photoexcitation. The dominant broader signals showing similar $|D|$ and $|E|$

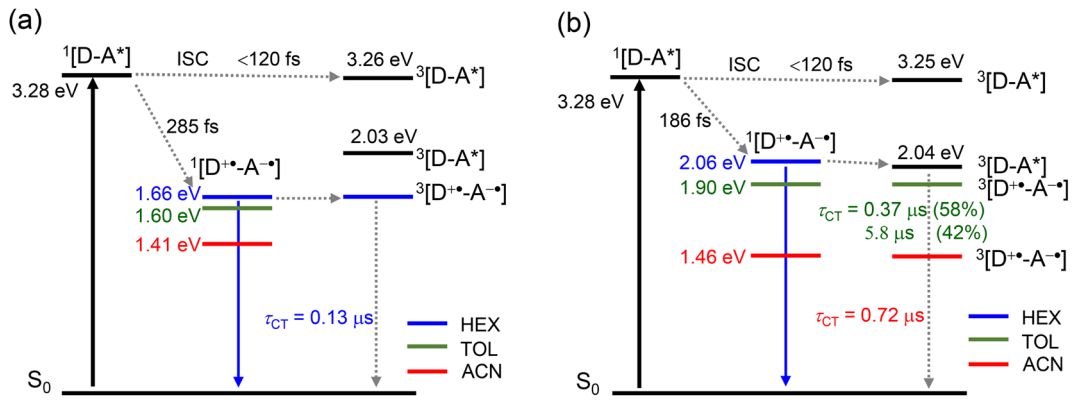

Scheme 2 Simplified Jablonski diagram illustrating the photophysical processes involved in (a) **Rho-NDI** and (b) **Rho-Ph-NDI**. The energy of the excited singlet states is derived from the spectroscopic data; the energy of CS states is obtained from electrochemical data; and the triplet state energy is approximated by TDDFT calculations at the B3LYP/6-31G(d) level using Gaussian 09. The number of the superscript denotes the spin multiplicity of the states.

values as compared to the triplet state of the native **NDI** are assigned to **NDI**-localized triplets formed *via* SOC-ISC. The weak and narrower signals in the middle of the spectra showing relatively small $|J|$ and $|D|$ values and $|E| = 0$ are assigned to the CS state. **Rho-NDI** features the largest value of dipolar interaction ($|D| = 184$ MHz) due to the smallest distance between Rho and **NDI** moieties compared with **Rho-Ph-NDI** ($|D| = 39$ MHz) and **Rho-PhMe-NDI** ($|D| = 41$ MHz). Moreover, for **Rho-NDI**, the time-dependent *e*,*a* → *a*,*e* phase change of the CS state spectrum is attributed to the population of the CS state from a singlet to a triplet state, respectively, which is evidence that the long-lived CS state results from the electron spin control effect.

Experimental section

General method

All chemicals used in synthesis are analytically pure. Solvents for synthesis were dried before using. UV-vis spectra were recorded using a UV-2550 spectrophotometer (Shimadzu Ltd., Japan). Fluorescence emission spectra were recorded using an FS5 spectrofluorometer (Edinburgh Instruments Ltd., U.K.). Fluorescence lifetimes were recorded using an OB920 luminescence lifetime spectrometer (Edinburgh Instrument Ltd., U.K.), and a picosecond EPL laser was used for excitation. Fluorescence quantum yields (Φ_F) were measured by using an absolute photoluminescence quantum yield spectrometer (Quantaurus-QY Plus C13534-11, Hamamatsu Ltd., Japan).

Synthesis of Rho-NDI

Under a N_2 atmosphere, compound **1** (37.9 mg, 0.10 mmol) and **4** (45.6 mg, 0.10 mmol) were dissolved in acetic acid (3 mL). The mixture was refluxed and stirred for 24 h. After the reaction was finished, the mixture was cooled to room temperature, and then ice water (10 mL) was added to the mixture. The pH of the resultant solution was adjusted to 8–9 by adding 1 M NaOH aqueous solution. A purple solid precipitate was formed and collected by filtration. The obtained solid was dried under vacuum at 50 °C. Then the crude product was purified by column chromatography (silica gel, EA : DCM = 1 : 20, v/v) to give a grey solid (25.2 mg, yield: 31%). M.p. 124.1–124.6 °C. ^{1}H NMR (400 MHz, DMSO-d_6): δ 8.61 (d, J = 7.6 Hz, 2H), 8.36 (d, J = 7.6 Hz, 2H), 8.03 (d, J = 7.6 Hz, 1H), 7.85–7.76 (m, 2H), 7.42 (d, J = 7.4 Hz, 1H), 6.51 (d, J = 8.9 Hz, 2H), 6.42 (m, 2H), 6.03 (s, 2H), 4.01–3.94 (m, 2H), 3.31–3.21 (m, 8H), 1.84–1.82 (m, 1H), 1.36–1.24 (m, 8H), 1.02–1.00 (m, 12H), 0.88–0.84 (m, 6H). ^{13}C NMR (125 MHz, DMSO-d_6): δ 163.11, 162.69, 159.51, 153.82, 148.48, 148.38, 133.88, 130.79, 130.36, 130.03, 129.76, 129.28, 127.15, 126.47, 125.67, 125.08, 124.73, 123.18, 107.90, 104.77, 96.74, 67.22, 43.64, 43.58, 31.18, 29.95, 28.90, 28.62, 28.59, 23.36, 22.34, 21.99, 13.83, 12.13, 10.33. HRMS (EI), m/z: $[M + H]^+$ calcd for $C_{50}H_{52}N_5O_6$: 818.3918; found: 818.3923.

Synthesis of Rho-Ph-NDI

Under a N_2 atmosphere, rhodamine B (120 mg, 0.27 mmol) was dissolved in dry DCM (7 mL), and then $POCl_3$ (0.2 mL) was added dropwise. The solution was refluxed and stirred for 5 h. The solvent was evaporated under reduced pressure, and then crude product was dissolved in dry CH_3CN (5 mL). The mixture was added dropwise to the solution of compound 2 (70.4 mg, 0.15 mmol) and Et_3N (0.3 mL) in CH_3CN (7 mL), and then the mixture was refluxed and stirred for 21 h. After the reaction was finished, the solvent was evaporated under reduced pressure, and the crude product was purified by column chromatography (silica gel, EA : DCM = 1 : 10, v/v) to give the product as a grey solid (72.4 mg, yield: 54%). M.p. 122.2–122.8 °C. ^{1}H NMR (400 MHz, $CDCl_3$): δ 8.77–8.72 (m, 4H), 8.01 (d, J = 7.6 Hz, 1H), 7.49–7.37 (m, 5H), 7.12–7.08 (m, 3H), 6.66 (s, 2H), 6.33 (d, J = 7.6 Hz, 3H), 4.20–4.09 (m, 2H), 3.33 (d, J = 7.6 Hz, 8H), 1.96–1.91 (m, 1H), 1.41–1.29 (m, 8H), 1.18–1.16 (m, 12H), 0.96–0.88 (m, 6H). ^{13}C NMR (150 MHz, $CDCl_3$): δ 168.26, 163.17, 162.85, 154.02, 152.76, 148.86, 137.92, 133.19, 131.26, 131.07, 129.62, 128.45, 126.99, 126.83, 126.71, 125.68, 123.75, 123.41, 108.33, 106.36, 98.00, 67.27, 44.65, 44.32, 37.94, 31.93, 30.71, 29.70, 29.66, 29.36, 28.63, 24.05, 23.04, 22.70, 14.07, 12.63, 10.60. HRMS (EI), m/z: $[M]^+$ calcd for $C_{56}H_{55}N_5O_6$: 893.4152; found: 893.4141.

Synthesis of Rho-PhMe-NDI

Under a N_2 atmosphere, rhodamine B (120 mg, 0.27 mmol) was dissolved in dry DCM (7 mL), and then $POCl_3$ (0.2 mL) was added dropwise. The solution was refluxed and stirred for 5 h. The solvent was evaporated under reduced pressure, and then the crude product was dissolved in dry CH_3CN (5 mL). The mixture was added to the solution of compound **3** (74.7 mg, 0.15 mmol) and Et_3N (0.3 mL) in CH_3CN (7 mL) dropwise under a N_2 atmosphere, and then the mixture was refluxed and stirred for 21 h. After the reaction was finished, the solvent was evaporated under reduced pressure, and the crude product was purified by column chromatography (silica gel, EA : DCM = 1 : 6, v/v) to give the product as a gray solid (70.6 mg, yield: 51%). M.p. 168.3–169.1 °C. ^{1}H NMR (400 MHz, $CDCl_3$): δ 8.80–8.77 (m, 4H), 8.07 (d, J = 6.2 Hz, 1H), 7.63–7.58 (m, 2H), 7.34–7.32 (m, 1H), 6.87 (s, 1H), 6.65–6.63 (m, 2H), 6.43–6.27 (m, 4H), 5.98 (s, 1H), 4.21–4.11 (m, 2H), 3.35–3.32 (m, 8H), 1.98–1.92 (m, 1H), 1.84 (s, 3H), 1.76 (s, 3H), 1.40–1.30 (m, 8H), 1.17–1.14 (m, 12H), 0.96–0.87 (m, 6H). ^{13}C NMR (125 MHz, $CDCl_3$): δ 165.74, 163.21, 162.12, 154.96, 153.94, 151.46, 148.95, 137.14, 135.32, 132.71, 131.40, 131.15, 131.05, 130.95, 129.95, 127.17, 126.89, 126.78, 124.46, 123.47, 108.20, 107.68, 107.30, 106.42, 98.01, 68.43, 44.65, 44.38, 37.95, 30.72, 29.70, 28.64, 24.06, 23.05, 18.07, 17.09, 14.08, 12.49, 10.62. HRMS (EI), m/z: $[M]^+$ calcd for $C_{58}H_{59}N_5O_6$: 921.4465; found: 921.4487.

Single crystal X-ray diffraction

A single crystal of **Rho-NDI** was obtained *via* slow diffusion of HEX into THF solution of the compound. The single-crystal X-ray diffraction data for **Rho-NDI** were collected on a Bruker D8 Venture CMOS-based diffractometer (Mo-Kα radiation, λ = 0.71073 Å) using the SMART and SAINT programs. Final unit cell parameters were based on all observed reflections from the integration of all frame data. The structures were solved with the ShelXT structure solution program using intrinsic phasing and refined with the ShelXL refinement package using least

squares minimization implanted in Olex2. All non-hydrogen atoms were refined anisotropically and the hydrogen atoms were located geometrically and fixed isotropic thermal parameters.

Electrochemical studies

The cyclic voltammetry curves were recorded with a CHI610D electrochemical workstation (CHI instruments, Inc., Shanghai, China). The counter electrode is a platinum electrode; a glassy carbon electrode is the working electrode. The ferrocenium/ferrocene (Fc^+/Fc) redox couple was used as an internal reference. Spectroelectrochemistry was performed using a 0.1 cm path length quartz electrochemical cell. A platinum gauze was the working electrode, and a platinum wire was the counter electrode. The potential was regulated with a CHI610D electrochemical workstation, and the spectra were recorded with an Agilent 8453 UV-vis spectroscopy system (Agilent Technologies Inc., USA). In both cases, $Bu_4N[PF_6]$ was used as the supporting electrolyte, and the $Ag/AgNO_3$ (0.1 M in ACN) couple was used as the reference electrode. Samples were deaerated with N_2 for *ca.* 15 min before measurement, and the N_2 atmosphere was kept during the measurement.

Femtosecond transient absorption spectroscopy

Ultrafast pump probe spectroscopy measurements were performed on a Ti:sapphire laser amplifier-optical parametric amplifier system (Spectra Physics, Spitfre Pro XP, TOPAS) and a commercial setup of an ultrafast transient absorption spectrometer (Spectra Physics, Helios). The global fitting and target analysis were carried out with a sequential model using Glotaran software.[79,80]

Nanosecond transient absorption spectroscopy

The nanosecond transient absorption spectra were studied on a LP920 laser flash photolysis spectrometer (Edinburgh Instruments, UK), and the signal was digitized with a Tektronix TDS 3012B oscilloscope. The samples were excited with a nanosecond pulsed laser (Quantel Nd: YAG nanosecond pulsed laser). The oxygen in the sample solution was removed by purging the solution with N_2 for 15 minutes before measurement. The typical laser power is 65 mJ per pulse at 355 nm. The data were analyzed with L900 software.

Steady-state and time-resolved electron paramagnetic resonance spectroscopy

Steady-state electron paramagnetic resonance (EPR) spectroscopy measurements were performed on an X-band (9.4 GHz) EPR ELEXSYS E500 spectrometer (Bruker, Germany) at 300 K. The radical anion of the compound was obtained by adding a reductant into deaerated *N*,*N*-dimethyl formamide (DMF), and then the EPR quartz tube was sealed with a H_2/O_2 torch under a N_2 atmosphere. Time-resolved (TR) EPR measurements were performed on an X-band EPR spectrometer based on a Bruker EMX (Germany) at 80 K and 298 K. Samples were dissolved in TOL/MeTHF (3 : 1, v/v). The oxygen was removed with five freeze–pump–thaw cycles. The spectra were simulated using the EasySpin package based on Matlab.[74]

DFT calculations

The geometries of the compounds, spin density surfaces, were optimized using density functional theory (DFT) with the B3LYP or CAM-B3LYP functional and 6-31G(d) basis set. There were no imaginary frequencies for all optimized structures. The triplet excited state energy of the compounds was calculated by time-dependent DFT (TDDFT) with the B3LYP functional and 6-31G(d) basis set based on the optimized ground-state geometry. The hyperfine coupling (HFC) constants were calculated using DFT with the UB3LYP functional and EPR-II basis set. All these calculations were performed with Gaussian 09.[81]

Data availability

All relevant data are presented in the main text and ESI.†

Author contributions

X. X., I. K. and P. M. contributed equally to this work.

Conflicts of interest

There are no conflicts to declare.

Acknowledgements

J. Z. thanks the NSFC (U2001222), the State Key Laboratory of Fine Chemicals, the Fundamental Research Funds for the Central Universities (DUT22LAB610) and the Department of Education of the Xinjiang Uyghur Autonomous Region (Tian-Shan Chair Professor) for financial support. M. F. and I. K. thank the Ministry of Science and Higher Education of the Russian Federation (Grant No. 075-15-2020-779).

Notes and references

1 J. W. Verhoeven, *J. Photochem. Photobiol., C*, 2006, **7**, 40–60.
2 J. W. Verhoeven, H. J. van Ramesdonk, M. M. Groeneveld, A. C. Benniston and A. Harriman, *ChemPhysChem*, 2005, **6**, 2251–2260.
3 M. A. Filatov, *Org. Biomol. Chem.*, 2020, **18**, 10–27.
4 D. M. Guldi, *Chem. Commun.*, 2000, 321–327.
5 N. Zarrabi, B. J. Bayard, S. Seetharaman, N. Holzer, P. Karr, S. Ciuti, A. Barbon, M. Di Valentin, A. van der Est, F. D'Souza and P. K. Poddutoori, *Phys. Chem. Chem. Phys.*, 2021, **23**, 960–970.
6 S. Suzuki, M. Kozaki, K. Nozaki and K. Okada, *J. Photochem. Photobiol., C*, 2011, **12**, 269–292.
7 S. Fukuzumi, *Pure Appl. Chem.*, 2007, **79**, 981–991.
8 E. Vauthey, *ChemPhysChem*, 2012, **13**, 2001–2011.
9 J. H. Golden, L. Estergreen, T. Porter, A. C. Tadle, M. R. Daniel Sylvinson, J. W. Facendola, C. P. Kubiak, S. E. Bradforth and M. E. Thompson, *ACS Appl. Energy Mater.*, 2018, **1**, 1083–1095.

10 H. Song, H. Zhao, Y. Guo, A. M. Philip, Q. Guo, M. Hariharan and A. Xia, *J. Phys. Chem. C*, 2020, **124**, 237–245.
11 S. Guo, K.-K. Chen, R. Dong, Z.-M. Zhang, J. Zhao and T.-B. Lu, *ACS Catal.*, 2018, **8**, 8659–8670.
12 C. K. Prier, D. A. Rankic and D. W. MacMillan, *Chem. Rev.*, 2013, **113**, 5322–5363.
13 D. P. Hari and B. König, *Chem. Commun.*, 2014, **50**, 6688–6699.
14 D. Ravelli, M. Fagnoni and A. Albini, *Chem. Soc. Rev.*, 2013, **42**, 97–113.
15 L. Shi and W. Xia, *Chem. Soc. Rev.*, 2012, **41**, 7687–7697.
16 H. Imahori, Y. Kobori and H. Kaji, *Acc. Mater. Res.*, 2021, **2**, 501–514.
17 K. Ohkubo, H. Kotani, J. Shao, Z. Ou, K. M. Kadish, G. Li, R. K. Pandey, M. Fujitsuka, O. Ito, H. Imahori and S. Fukuzumi, *Angew. Chem., Int. Ed.*, 2004, **43**, 853–856.
18 T. Higashino, T. Yamada, M. Yamamoto, A. Furube, N. V. Tkachenko, T. Miura, Y. Kobori, R. Jono, K. Yamashita and H. Imahori, *Angew. Chem., Int. Ed.*, 2016, **55**, 629–633.
19 A. Karimata, S. Suzuki, M. Kozaki, K. Kimoto, K. Nozaki, H. Matsushita, N. Ikeda, K. Akiyama, D. Kosumi, H. Hashimoto and K. Okada, *J. Phys. Chem. A*, 2014, **118**, 11262–11271.
20 D. I. Schuster, P. Cheng, P. D. Jarowski, D. M. Guldi, C. Luo, L. Echegoyen, S. Pyo, A. R. Holzwarth, S. E. Braslavsky, R. M. Williams and G. Klihm, *J. Am. Chem. Soc.*, 2004, **126**, 7257–7270.
21 K.-Y. Chen, C.-C. Hsieh, Y.-M. Cheng, C.-H. Lai, P.-T. Chou and T. J. Chow, *J. Phys. Chem. A*, 2006, **110**, 12136–12144.
22 H. Imahori, D. M. Guldi, K. Tamaki, Y. Yoshida, C. Luo, Y. Sakata and S. Fukuzumi, *J. Am. Chem. Soc.*, 2001, **123**, 6617–6628.
23 H. Imahori, Y. Sekiguchi, Y. Kashiwagi, T. Sato, Y. Araki, O. Ito, H. Yamada and S. Fukuzumi, *Chem.–Eur. J.*, 2004, **10**, 3184–3196.
24 Y. Hou, X. Zhang, K. Chen, D. Liu, Z. Wang, Q. Liu, J. Zhao and A. Barbon, *J. Mater. Chem. C*, 2019, **7**, 12048–12074.
25 S. Suzuki, R. Sugimura, M. Kozaki, K. Keyaki, K. Nozaki, N. Ikeda, K. Akiyama and K. Okada, *J. Am. Chem. Soc.*, 2009, **131**, 10374–10375.
26 B. Geiβ and C. Lambert, *Chem. Commun.*, 2009, 1670–1672.
27 S.-H. Lee, C. T.-L. Chan, K. M.-C. Wong, W. H. Lam, W.-M. Kwok and V. W.-W. Yam, *J. Am. Chem. Soc.*, 2014, **136**, 10041–10052.
28 A. Karimata, H. Kawauchi, S. Suzuki, M. Kozaki, N. Ikeda, K. Keyaki, K. Nozaki, K. Akiyama and K. Okada, *Chem. Lett.*, 2013, **42**, 794–796.
29 X. Zhang, X. Chen and J. Zhao, *Dalton Trans.*, 2021, **50**, 59–67.
30 J. Hankache and O. S. Wenger, *Chem. Commun.*, 2011, **47**, 10145–10147.
31 Z. E. X. Dance, Q. Mi, D. W. McCamant, M. J. Ahrens, M. A. Ratner and M. R. Wasielewski, *J. Phys. Chem. B*, 2006, **110**, 25163–25173.
32 M. T. Colvin, R. Carmieli, T. Miura, S. Richert, D. M. Gardner, A. L. Smeigh, S. M. Dyar, S. M. Conron, M. A. Ratner and M. R. Wasielewski, *J. Phys. Chem. A*, 2013, **117**, 5314–5325.
33 S. Chakraborty, T. J. Wadas, H. Hester, R. Schmehl and R. Eisenberg, *Inorg. Chem.*, 2005, **44**, 6865–6878.
34 D. Anglos, V. Bindra and A. Kuki, *J. Chem. Soc., Chem. Commun.*, 1994, 213–215.
35 S. Fukuzumi, H. Kotani, K. Ohkubo, S. Ogo, N. V. Tkachenko and H. Lemmetyinen, *J. Am. Chem. Soc.*, 2004, **126**, 1600–1601.
36 S. I. van Dijk, C. P. Groen, F. Hartl, A. M. Brouwer and J. W. Verhoeven, *J. Am. Chem. Soc.*, 1996, **118**, 8425–8432.
37 L. Hviid, A. M. Brouwer, M. N. Paddon-Row and J. W. Verhoeven, *ChemPhysChem*, 2001, **2**, 232–235.
38 M. Murakami, K. Ohkubo, T. Nanjo, K. Souma, N. Suzuki and S. Fukuzumi, *ChemPhysChem*, 2010, **11**, 2594–2605.
39 D. Liu, A. M. El-Zohry, M. Taddei, C. Matt, L. Bussotti, Z. Wang, J. Zhao, O. F. Mohammed, M. Di Donato and S. Weber, *Angew. Chem., Int. Ed.*, 2020, **59**, 11591–11599.
40 D. J. Gibbons, A. Farawar, P. Mazzella, S. Leroy-Lhez and R. M. Williams, *Photochem. Photobiol. Sci.*, 2020, **19**, 136–158.
41 X. Chen, A. A. Sukhanov, Y. Yan, D. Bese, C. Bese, J. Zhao, V. K. Voronkova, A. Barbon and H. G. Yaglioglu, *Angew. Chem., Int. Ed.*, 2022, e202203758.
42 M. Hu, A. A. Sukhanov, X. Zhang, A. Elmali, J. Zhao, S. Ji, A. Karatay and V. K. Voronkova, *J. Phys. Chem. B*, 2021, **125**, 4187–4203.
43 Y. Cheng, L. Li, F. Wei and K. M.-C. Wong, *Inorg. Chem.*, 2018, **57**, 6439–6446.
44 G. P. Wiederrecht, W. A. Svec, M. R. Wasielewski, T. Galili and H. Levanon, *J. Am. Chem. Soc.*, 2000, **122**, 9715–9722.
45 Y. Mori, Y. Sakaguchi and H. Hayashi, *J. Phys. Chem. A*, 2002, **106**, 4453–4467.
46 N. Pearce, E. S. Davies, R. Horvath, C. R. Pfeiffer, X.-Z. Sun, W. Lewis, J. McMaster, M. W. George and N. R. Champness, *Phys. Chem. Chem. Phys.*, 2018, **20**, 752–764.
47 N. J. Turro, V. Ramamurthy and J. C. Scaiano, *Principles of molecular photochemistry: an introduction*, University Science Books, 2009.
48 Z. Wang, J. Zhao, M. Di Donato and G. Mazzone, *Chem. Commun.*, 2019, **55**, 1510–1513.
49 X. Xiao, J. Pang, A. A. Sukhanov, Y. Hou, J. Zhao, M.-D. Li and V. K. Voronkova, *J. Chem. Phys.*, 2020, **153**, 184312.
50 S. Sasaki, K. Hattori, K. Igawa and G.-i. Konishi, *J. Phys. Chem. A*, 2015, **119**, 4898–4906.
51 G. Tang, A. A. Sukhanov, J. Zhao, W. Yang, Z. Wang, Q. Liu, V. K. Voronkova, M. Di Donato, D. Escudero and D. Jacquemin, *J. Phys. Chem. C*, 2019, **123**, 30171–30186.
52 X. Zhang, X. Liu, M. Taddei, L. Bussotti, I. Kurganskii, M. Li, X. Jiang, L. Xing, S. Ji, Y. Huo, J. Zhao, M. Di Donato, Y. Wan, Z. Zhao and M. V. Fedin, *Chem.–Eur. J.*, 2022, **28**, e202200510.
53 X. Cui, J. Zhao, Z. Lou, S. Li, H. Wu and K.-l. Han, *J. Org. Chem.*, 2015, **80**, 568–581.
54 L. Yuan, W. Lin, Y. Xie, B. Chen and S. Zhu, *J. Am. Chem. Soc.*, 2012, **134**, 1305–1315.

55 X. Zhang, L. Chen, Z. Huang, N. Ling and Y. Xiao, *Chem.–Eur. J.*, 2021, **27**, 3688–3693.
56 K. Chen, J. Zhao, X. Li and G. G. Gurzadyan, *J. Phys. Chem. A*, 2019, **123**, 2503–2516.
57 H. Matsuoka, Y. Shibano, I. Akimoto and Y. Kanzaki, *Bull. Chem. Soc. Jpn.*, 2022, **95**, 59–63.
58 R. Ziessel, B. D. Allen, D. B. Rewinska and A. Harriman, *Chem.–Eur. J.*, 2009, **15**, 7382–7393.
59 H. Imahori, K. Hagiwara, M. Aoki, T. Akiyama, S. Taniguchi, T. Okada, M. Shirakawa and Y. Sakata, *J. Am. Chem. Soc.*, 1996, **118**, 11771–11782.
60 S. Guha, F. S. Goodson, S. Roy, L. J. Corson, C. A. Gravenmier and S. Saha, *J. Am. Chem. Soc.*, 2011, **133**, 15256–15259.
61 O. Yushchenko, G. Licari, S. Mosquera-Vazquez, N. Sakai, S. Matile and E. Vauthey, *J. Phys. Chem. Lett.*, 2015, **6**, 2096–2100.
62 A. C. Marco Montalti, L. Prodi and M. Teresa Gandolfi, *Handbook of Photochemistry*, CRC Press, Boca Raton, 2006.
63 C. Luo, D. M. Guldi, H. Imahori, K. Tamaki and Y. Sakata, *J. Am. Chem. Soc.*, 2000, **122**, 6535–6551.
64 S. Guha and S. Saha, *J. Am. Chem. Soc.*, 2010, **132**, 17674–17677.
65 S. Guha, F. S. Goodson, L. J. Corson and S. Saha, *J. Am. Chem. Soc.*, 2012, **134**, 13679–13691.
66 V. V. Roznyatovskiy, D. M. Gardner, S. W. Eaton and M. R. Wasielewski, *Org. Lett.*, 2014, **16**, 696–699.
67 Y. Hou, I. Kurganskii, A. Elmali, H. Zhang, Y. Gao, L. Lv, J. Zhao, A. Karatay, L. Luo and M. Fedin, *J. Chem. Phys.*, 2020, **152**, 114701.
68 K. Chen, I. V. Kurganskii, X. Zhang, A. Elmali, J. Zhao, A. Karatay and M. V. Fedin, *Chem.–Eur. J.*, 2021, **27**, 7572–7587.
69 N. Rehmat, I. V. Kurganskii, Z. Mahmood, Q. L. Guan, J. Zhao, Y. H. Xing, G. G. Gurzadyan and M. V. Fedin, *Chem.–Eur. J.*, 2021, **27**, 5521–5535.
70 M. T. Colvin, A. B. Ricks, A. M. Scott, A. L. Smeigh, R. Carmieli, T. Miura and M. R. Wasielewski, *J. Am. Chem. Soc.*, 2011, **133**, 1240–1243.
71 M. T. Colvin, A. B. Ricks, A. M. Scott, D. T. Co and M. R. Wasielewski, *J. Phys. Chem. A*, 2012, **116**, 1923–1930.
72 T. Fukuju, H. Yashiro, K. Maeda, H. Murai and T. Azumi, *J. Phys. Chem. A*, 1997, **101**, 7783–7786.
73 C. D. Buckley, D. A. Hunter, P. J. Hore and K. A. McLauchlan, *Chem. Phys. Lett.*, 1987, **135**, 307–312.
74 S. Stoll and A. Schweiger, *J. Magn. Reson.*, 2006, **178**, 42–55.
75 K. Hasharoni, H. Levanon, S. R. Greenfield, D. J. Gosztola, W. A. Svec and M. R. Wasielewski, *J. Am. Chem. Soc.*, 1995, **117**, 8055–8056.
76 K. Hasharoni, H. Levanon, S. R. Greenfield, D. J. Gosztola, W. A. Svec and M. R. Wasielewski, *J. Am. Chem. Soc.*, 1996, **118**, 10228–10235.
77 R. Carmieli, A. L. Smeigh, S. M. Mickley Conron, A. K. Thazhathveetil, M. Fuki, Y. Kobori, F. D. Lewis and M. R. Wasielewski, *J. Am. Chem. Soc.*, 2012, **134**, 11251–11260.
78 M. D. E. Forbes, L. E. Jarocha, S. Sim and V. F. Tarasov, *Adv. Phys. Org. Chem.*, 2013, **47**, 1–83.
79 I. H. M. van Stokkum, D. S. Larsen and R. van Grondelle, *Biochim. Biophys. Acta, Bioenerg.*, 2004, **1657**, 82–104.
80 J. Snellenburg, S. Laptenok, R. Seger, K. Mullen, I. Van Stokkum, J. J. Snellenburg, S. Laptenok, R. Seger, K. M. Mullen and I. H. M. van Stokkum, *J. Stat. Software*, 2012, **49**, 1–22.
81 M. J. Frisch, G. W. Trucks, H. B. Schlegel, G. E. Scuseria, M. A. Robb, J. R. Cheeseman, G. Scalmani, V. Barone, B. Mennucci, G. A. Petersson, H. Nakatsuji, M. Caricato, X. Li, H. P. Hratchian, A. F. Izmaylov, J. Bloino, G. Zheng, J. L. Sonnenberg, M. Hada, M. Ehara, K. Toyota, R. Fukuda, J. Hasegawa, M. Ishida, T. Nakajima, Y. Honda, O. Kitao, H. Nakai, T. Vreven, J. A. Montgomery Jr., J. E. Peralta, F. Ogliaro, M. Bearpark, J. J. Heyd, E. Brothers, K. N. Kudin, V. N. Staroverov, R. Kobayashi, J. Normand, K. Raghavachari, A. Rendell, J. C. Burant, S. S. Iyengar, J. Tomasi, M. Cossi, N. Rega, J. M. Millam, M. Klene, J. E. Knox, J. B. Cross, V. Bakken, C. Adamo, J. Jaramillo, R. Gomperts, R. E. Stratmann, O. Yazyev, A. J. Austin, R. Cammi, C. Pomelli, J. W. Ochterski, R. L. Martin, K. Morokuma, V. G. Zakrzewski, G. A. Voth, P. Salvador, J. J. Dannenberg, S. Dapprich, A. D. Daniels, O. Farkas, J. B. Foresman, J. V. Ortiz, J. Cioslowski, and D. J. Fox, *Gaussian, Gaussian 09 (Revision A.01)*, Gaussian, Inc., Wallingford CT, 2009.